



HAL
open science

Dates and rates of endo-exorheic drainage development: Insights from fluvial terraces (Duero River, Iberian Peninsula)

Laura Rodríguez-Rodríguez, Loreto Antón, Ángel Rodés, Raimon Pallàs,
Daniel García-Castellanos, Ivone Jiménez-Munt, Lucía Struth, Laëtitia
Leanni, A.S.T.E.R. Team, Georges Aumaitre, et al.

► To cite this version:

Laura Rodríguez-Rodríguez, Loreto Antón, Ángel Rodés, Raimon Pallàs, Daniel García-Castellanos, et al.. Dates and rates of endo-exorheic drainage development: Insights from fluvial terraces (Duero River, Iberian Peninsula). *Global and Planetary Change*, 2020, 193, pp.103271. 10.1016/j.gloplacha.2020.103271 . hal-03153524

HAL Id: hal-03153524

<https://hal.science/hal-03153524v1>

Submitted on 22 Aug 2022

HAL is a multi-disciplinary open access archive for the deposit and dissemination of scientific research documents, whether they are published or not. The documents may come from teaching and research institutions in France or abroad, or from public or private research centers.

L'archive ouverte pluridisciplinaire **HAL**, est destinée au dépôt et à la diffusion de documents scientifiques de niveau recherche, publiés ou non, émanant des établissements d'enseignement et de recherche français ou étrangers, des laboratoires publics ou privés.



Distributed under a Creative Commons Attribution - NonCommercial 4.0 International License

1 **DATES AND RATES OF ENDO-EXORHEIC DRAINAGE DEVELOPMENT:**
2 **INSIGHTS FROM FLUVIAL TERRACES (DUERO RIVER, IBERIAN**
3 **PENINSULA)**

4 **Laura Rodríguez-Rodríguez^{1,2*}, Loreto Antón³, Ángel Rodés⁴, Raimon Pallàs⁵,**
5 **Daniel García-Castellanos⁶, Ivone Jiménez-Munt⁶, Lucía Struth⁶, Laëtítia Leanni⁷,**
6 **ASTER Team⁷**

7 ¹ Departamento de Ciencias de la Tierra y Física de la Materia Condensada,
8 Universidad de Cantabria, Avenida de los Castros 48, 93005 Santander, Spain.

9 ² Laboratoire de Géographie Physique (UMR 8591, CNRS), 1 Place Aristide Briand
10 92195 Meudon, France.

11 ³ Universidad Nacional de Educación a Distancia (UNED), Departamento de Ciencias
12 Analíticas, Senda del Rey 9, Madrid, Spain.

13 ⁴ NERC Cosmogenic Isotope Analysis Facility, Scottish Universities Environmental
14 Research Centre, East Kilbride G75 0QF United Kingdom.

15 ⁵ Institut de Recerca Geomodels, RISKNAT Group, Departament de Dinàmica de la
16 Terra i de l'Oceà, Universitat de Barcelona, Martí i Franques s/n, Barcelona, Spain.

17 ⁶ Institut de Ciències de la Terra Jaume Almera, ICTJA-CSIC, Solé i Sabaris s/n,
18 Barcelona, Spain.

19 ⁷Aix Marseille Université, CNRS, IRD, INRA, Coll France, UM34 CEREGE,
20 Technopôle de l'Environnement Arbois-Méditerranée, BP80,13545 Aix-en-Provence,
21 France. [ASTER Team: Georges Aumaître, Didier Bourlès, Karim Keddadouche]

22 * laura.rodriquezr@unican.es (Corresponding author: L. Rodríguez-Rodríguez)

23 **Abstract**

24 Fluvial terraces are valuable records to study and characterize landscape evolution and
25 river response to base level lowering, and to decipher coupled responses between fluvial
26 incision and regional tectonics. The opening of closed basins has a strong impact on
27 fluvial dynamics, as it involves an abrupt base level lowering that accelerates landscape
28 fluvial dissection. This study focuses on the time response of the Duero Basin, the
29 largest and best preserved among the Cenozoic basins of the Iberian Peninsula, to
30 exorheism. Fluvial incision due to basin opening has developed up to 13 un-paired
31 strath terraces along the south margin of the Duero river, distributed at relative heights
32 up to +136–128 m compared to the modern floodplain. Paired ^{10}Be – ^{26}Al cosmogenic
33 isotope depth profiles from six fluvial terraces, located ca. 30 to 80 km upstream from
34 the opening zone, suggest Pleistocene ages for almost the entire fluvial terrace staircase
35 (from T3 at +112–107 m, to T12 at +13–11 m). The terrace density and the total
36 lowering of the terrace surface, key parameters in limiting terrace exposure ages, were
37 estimated based on field and geomorphological data. Apparent burial durations and
38 basin denudation rates deduced from inherited ^{10}Be – ^{26}Al concentrations provide
39 valuable information on basin evolution. Apparent basin denudation rates remained
40 relatively low ($<3\text{--}6\text{ m}\cdot\text{Ma}^{-1}$) during the Pliocene, and doubled ($8\text{--}13\text{ m}\cdot\text{Ma}^{-1}$) during
41 the Early Pleistocene (ca. 2–1 Ma) possibly showing a lower proportion of recycled
42 sediments. Time averaged incision rates deduced from terraces in the study area and
43 along some tributaries show that incision rates are higher close to the opening site (122
44 to $<250\text{ m}\cdot\text{Ma}^{-1}$) than towards the upstream part of the catchment ($88\text{--}68\text{ m}\cdot\text{Ma}^{-1}$),
45 evidencing the retrogressive travel of the erosive wave nucleated at the opening site.

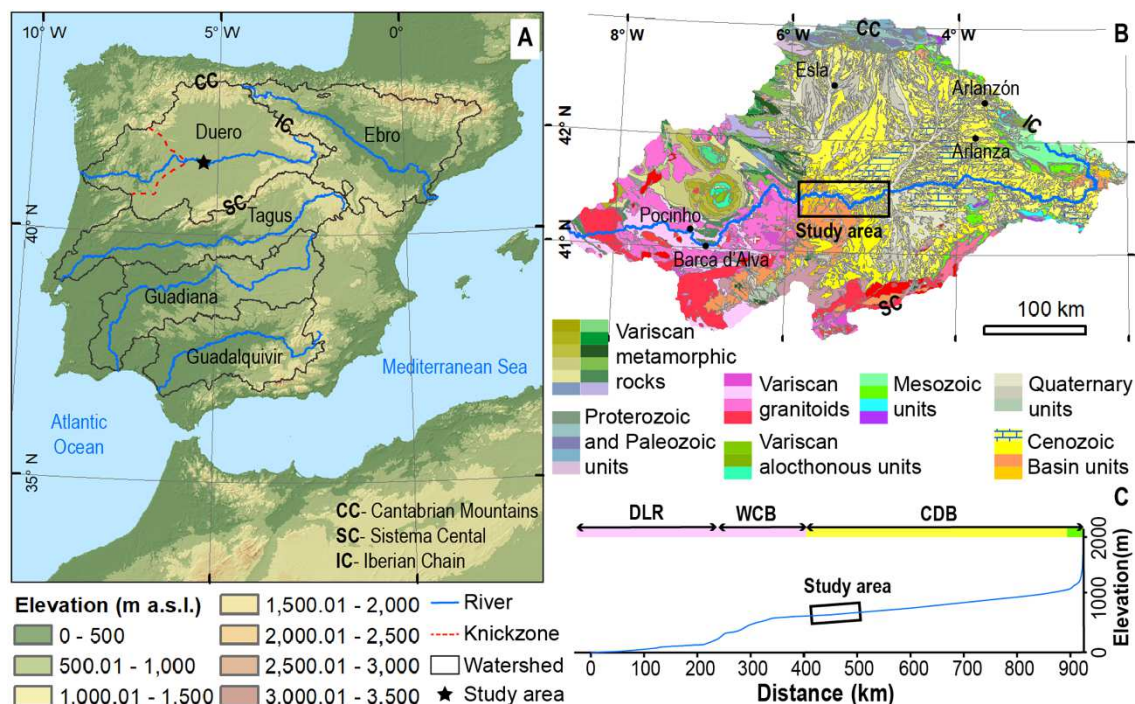
46 **1. Introduction**

47 Endorheic basins (also named closed, intermountain, or internally-drained basins)
48 are depressions lacking any water outflow towards the ocean. They constitute valuable
49 records for understanding the evolution and dynamics of surface processes on a range of
50 spatial scales, as they trap sediments until they eventually become externally drained
51 (exorheic), then excavating and exposing their sedimentary record and forming
52 planation surfaces and fluvial terraces, which allows deciphering landscape evolution
53 (García-Castellanos et al., 2003; Yu et al., 2014; He et al., 2017). Investigating how
54 basins evolve after an endo-exorheic transition is key for understanding long-term
55 landscape evolution (at geologic timescale) and for elucidating the mechanisms by
56 which large basins recover a steady state profile. This is most dramatically expressed in
57 the event of large drainage changes caused by fluvial captures, by sediment/water
58 overfilling of basins that leads to basin spillover, or by a combination of these
59 mechanisms (Spencer and Pearthree, 2001; García-Castellanos and Larrasoña, 2015;
60 Richardson et al., 2008; Heidarzadeh et al., 2017). For example, based on apatite
61 fission track analysis and stratigraphic sections, Richardson et al. (2008) found that the
62 Sichuan Basin (central China) underwent accelerated widespread erosion of 1 to 4 km
63 of overlying sedimentary material after the Yangtze River started excavating the Three
64 Gorges. Similarly, the Ebro Basin (NE Spain) underwent the excavation of up to a
65 kilometer of sediment after its endorheic lake system was captured by or spilled over
66 the Ebro River ca. 8-12 Ma ago (García-Castellanos et al., 2003). Fluvial terrace
67 architecture is key to understand how fast large basins might respond after an endo-
68 exorheic transition and which factors control how the wave of incision is transmitted
69 upstream. The review work of Demoulin et al. (2017) stands out that fluvial terrace
70 patterns and timing of fluvial incision are essential information to isolate the effects of
71 other driving factors for erosion that might be also involved in terrace formation such as
72 tectonics, climate variations, and other non-tectonic factors (such as bedrock lithology).
73 However, few studies focus on continental-scale drainage reorganization and, within
74 those, most studies lack rigorous age control to allow accurate insights into erosion rates
75 and the timing of large-scale landscape modification.

76 The Iberian Peninsula is known for the occurrence of several large-scale foreland
77 basins formed during the Alpine Orogeny that evolved as closed basins during a
78 significant part of the Cenozoic (Friend and Dabrio, 1996). These basins later became
79 externally drained towards the Atlantic Ocean and the Mediterranean Sea, exposing

80 their infill sequences by fluvial down-cutting in response to basin opening (Figure 1).
81 Santisteban and Schulte (2007) reviewed fluvial terrace patterns in the major Iberian
82 basins (Duero, Ebro, Tagus, Guadalquivir and Guadiana) and concluded that the time of
83 incision and river response to basin opening is highly variable depending on
84 local/regional climate, glacio-eustatic sea-level changes, and local/regional tectonics.
85 Hence, while some basins such as the Ebro Basin have suffered remarkable erosion of
86 their infill sequence (García-Castellanos and Larrasoña, 2015), others remain relatively
87 intact. For example, the Duero Basin stands a transient river profile since the endo-
88 exorheic transition (Antón et al., 2012, 2014; Figure 1), recording scarce total
89 denudation due to fluvial entrenchment caused by base level lowering (Antón et al.,
90 2019). A cross comparison between the morphometric indices and knickpoint
91 distribution in the Ebro and Duero basins suggests a short-term aggressive role of the
92 Ebro network (responsible for the westward migration observed in the water divide that
93 separates both basins), but a large-scale aggressor role for the Duero over the Ebro in
94 the long-term based on chi-analysis (Struth et al., 2019). Particularly, the Duero river
95 displays two trains of knickpoints that propagate differently through the soft Cenozoic
96 sediment cover and the Paleozoic crystalline bedrock (Struth et al., 2019), consistently
97 with the few incision rates available in the Arlanzón and Esla tributaries (Moreno et al.,
98 2012; Schaller et al., 2016a). Either a younger opening age for the Duero Basin
99 compared to other Iberian basins (> 3 Ma according to Antón et al., 2019; ~3.7–1.8 Ma
100 according to Cunha et al., 2019; 1.1–1.9 Ma according to Silva et al., 2017) and/or the
101 resistant lithology that configures the Duero basin fringe (Struth et al., 2019) could
102 explain the differences observed in fluvial entrenchment in response to sudden base-
103 level lowering caused by an endo-exorheic transition. Here, we target a sequence of
104 thirteen inset fluvial strath terraces formed in response to the Duero endo-exorheic
105 transition, which are now hanging at heights up to +136–128 m above the modern
106 floodplain (Rodríguez-Rodríguez et al., 2020; Figure 2). The sequence is preserved at
107 the western end of the Cenozoic Duero Basin (CDB), along the 90 km-long reach
108 placed ca. 30 km upstream from the major Arribes knickzone (Figure 1). The Arribes
109 knickzone is excavated in the Paleozoic crystalline bedrock, along the WCB (Western
110 fringe of the Cenozoic Basin) which separates the Duero Lower Reach (DLR) from the
111 Cenozoic sedimentary infill of the CDB (Antón et al. 2012; Figure 1). We fitted the
112 Combined Surface Exposure-Burial Dating (CSEB) model to our ^{10}Be and ^{26}Al depth-
113 profile data in order to produce a numerical geochronology of six terraces belonging to

114 the Duero fluvial staircase, allowing us to discuss: (i) terrace depositional ages; (ii)
 115 changes in denudation rates at basin scale over time; (iii) fluvial incision rates in
 116 response to base level lowering and fluvial entrenchment, and (iv) discuss the upstream
 117 transmission of the erosion wave caused by the endo-exorheic transition.

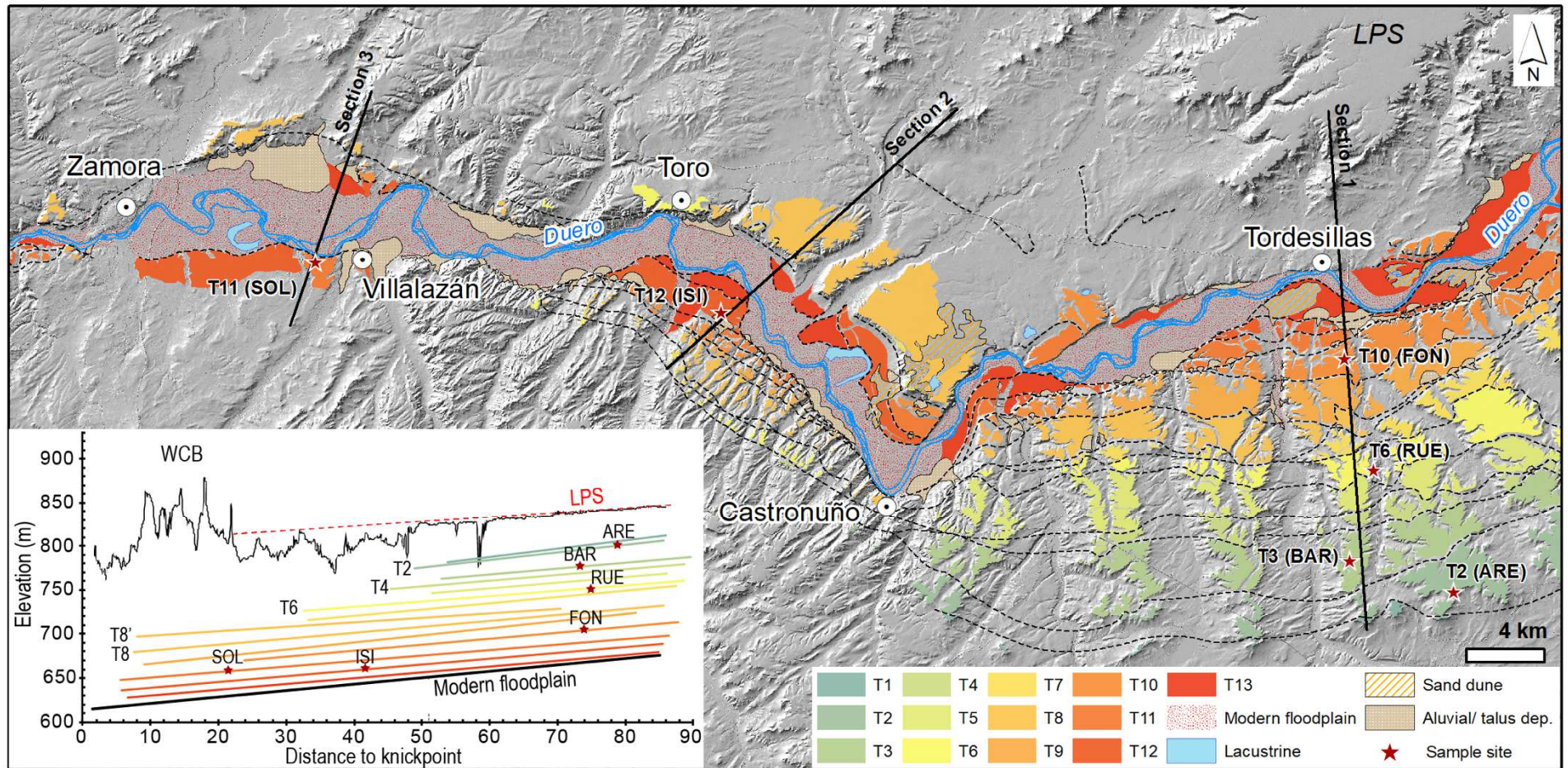


118
 119 Figure 1.- The Cenozoic Duero Basin (CDB) is the largest Iberian basin that best-
 120 preserves both the pre-opening topography and the endorheic sedimentary infill
 121 sequence (Antón et al., 2012, 2019). The CDB is limited by the Cantabrian Mountains
 122 to the north, the Iberian Chain to the east, the Sistema Central to the south, and the
 123 Western fringe of the Cenozoic Basin to the west (WCB). The transient long-profile of
 124 the Duero river shows a knickzone along the WCB (excavated in the Paleozoic
 125 crystalline bedrock), which separates the Duero Lower Reach (DLR) from the Cenozoic
 126 sedimentary infill of the CDB (mostly composed by alluvial detrital conglomerate and
 127 sandstone capped by lacustrine carbonate and evaporitic units). Geologic map source:
 128 http://mapas.igme.es/gis/rest/services/Cartografia_Geologica/IGME_EP_Geologico_1
 129 M_2018/MapServer (last accessed on April 2020).

130 2. Geologic and geomorphologic background of the study area

131 The Duero Basin is the largest among the Iberian Cenozoic basins: ~50000 km² in
 132 sediment-covered area and 90400 km² in total catchment area (Antón et al., 2019). It
 133 acted as foreland basin for the Cantabrian Mountains during the Eocene (Alonso et al.,
 134 1996) and for the Sistema Central between the Oligocene and Miocene (Capote et al.,
 135 2002), accumulating as much as 3 km of sediments (Gómez-Ortiz et al., 2005). The

136 youngest geologic formation sedimented in endorheic conditions, named the Páramo
137 Formation, is mostly composed by extensive carbonate facies (mostly limestone, marl
138 and gypsum) that suggests major expansion of lake environments at the basin's
139 depocenter during the middle and upper Miocene (Alonso-Zarza et al., 2002). Based on
140 magnetostratigraphic analysis, the top of the Páramo Formation was assigned a
141 Tortonian age (9.7–9.6 Ma according to Krijgsman et al., 1996; ~9.1 Ma according to
142 Beamoud et al., 2006). In contrast, mammal assemblages found at the youngest
143 carbonate unit of this formation (the Upper Páramo Limestone, or UPL) yielded
144 Vallesian ages in the southwest part of the basin (where the record is less complete),
145 while Turolian ages have been reported for fluvial deposits near the base of the
146 sequence at the basin center, which might point to a Pliocene age for the top of the UPL
147 (Alonso-Gavilan et al., 1989; Mediavilla and Dabrio, 1989; Alonso-Zarza et al., 2002
148 and references therein). However, Santisteban et al. (1997) have interpreted these
149 fluvial deposits as related to the first stages of fluvial dissection already in exorheic
150 conditions. A detailed analysis of erosion surfaces in the eastern sector of the basin
151 (Sierra de Atapuerca in the Iberian Chain) reveals up to four erosional surfaces, the
152 youngest formed after the Duero Basin opened to the Atlantic (Benito-Calvo and Pérez-
153 González, 2007). It laterally connects with the Lower Páramo Surface (LPS in Figure
154 2), developed on top of the Lower Páramo Limestone unit (or LPL) due to differential
155 exposure in response to fluvial dissection after the basin opening during the Pliocene-
156 Pleistocene (Benito-Calvo and Pérez-González, 2007). An opening age of ~1.1 to 1.9
157 Ma has been proposed based on a cross-comparison between the fluvial terrace
158 staircases preserved in the Duero and the Tagus basins, henceforth attributing the full
159 sequence of fluvial terraces to the Pleistocene (Silva et al., 2017). However, the age-
160 height transfer curve reported for the Duero river in their work was supported on the
161 few numerical ages available for the Arlanzón tributary, close to the source area of
162 sediments in the Iberian Chain (Figure 1). Finally, an older opening age range of ~3.7–
163 1.8 Ma has been recently reported based on an extrapolation of incision rates derived
164 from strath terraces hanging at +53–48 m (360–>230 ka), +34–27 m (57 ka) and +17–
165 13 m (39–12 ka) between Pocinho and Barca d'Alva (Cunha et al., 2019), downstream
166 of the Arribes knickzone, in the upper end of the Duero Lower Reach (DLR; Figure 1).



167

168 Figure 2.- Geomorphological map of the fluvial terrace staircase developed by the Duero River upstream the Arribes knickpoint. Terrace sample
 169 site locations are shown both in the map and along the reconstructed former river profiles based on statistical analysis of terrace surface points
 170 extracted from a high-resolution digital elevation model (Rodríguez-Rodríguez et al., 2020). The swath profile of maximum elevation shows the
 171 topographic signature of the LPS erosional surface, presumably linked to the initial emptying of the basin after the endo-exorheic transition.

172 Although the precise location of the opening point for the CDB drainage is
173 unknown, there is a general consensus about its location at the WCB (Silva et al., 2017
174 and references therein; Figure 1). This work refers to an opening area located at the
175 Arribes knickzone (ca. 20-50 km downstream from Zamora; Figure 2) where resistant
176 bedrock, composed by igneous and metamorphic rocks, controls the initiation and
177 progression of the continental scale drainage reorganization at the uppermost CDB (e.g.
178 Struth et al., 2019). The study area covers the lowermost 90 km-long reach of the upper
179 Duero river placed immediately upstream the Arribes knickzone, in the Spanish regions
180 of Valladolid and Zamora. Modern climate is characterized by mean annual
181 precipitation of 366–478 mm (<https://sig.mapama.gob.es/siga/>, accessed on August
182 2019), with a marked dry season in summer. Mean annual temperature is ~12 °C,
183 annually displaying less than 49 days of winter temperatures equal or below 0°C (mean
184 temperature minima values in January are 2.5–5°C) and reaching maxima temperature
185 values in the range 22.5–25°C during the summer season
186 ([http://www.aemet.es/es/serviciosclimaticos/datosclimatologicos/atlas_climatico/visor_](http://www.aemet.es/es/serviciosclimaticos/datosclimatologicos/atlas_climatico/visor_atlas_climatico#enlaces_asociados)
187 [atlas_climatico#enlaces_asociados](http://www.aemet.es/es/serviciosclimaticos/datosclimatologicos/atlas_climatico/visor_atlas_climatico#enlaces_asociados), last accessed on April 2020). Fluvial terraces crop
188 out as un-paired strath terraces formed by incision of the Duero River in the endorheic
189 infill sequence in response to the base level lowering linked to the endo-exorheic
190 transition, forming successive bedrock stairs capped with fluvial sediments up to 2–7 m
191 thick. The elevation difference between the LPS (preserved in the north margin of the
192 river) and the modern floodplain suggests that total incision overcomes 180 m (Figure
193 2). Fluvial terraces are preferentially preserved along the south margin of the river,
194 extending as far as 18 km south from the modern channel and hanging above the
195 modern floodplain at relative heights of: +136–128 m (T1); +130–124 m (T2); +110–
196 109 m (T3); +104–101 m (T4); +95–91 m (T5); +88–81 m (T6); c. +77 m (T7); +79–59
197 m (T8’); +60–55 m (T8); +51–44 m (T9); +40–35 m (T10); +30–10 m (T11); +18–12 m
198 (T12); and +9–3 m (T13; Rodríguez-Rodríguez et al., 2020). The staircase sequence is
199 fully represented in the eastern half of the study area, east of Castronuño village, while
200 only the intermediate and lowest terrace levels are present between Castronuño and the
201 Arribes knickzone. This pattern is possibly related to the occurrence of higher incision
202 rates close to the opening site than those recorded upstream over the time period when
203 terraces T1 to T9 were being deposited. This would explain the more extensive terrace
204 remnants and the higher number of terrace levels upstream Castronuño than between
205 Castronuño and the Arribes knickzone. Fluvial long-profiles reconstructed through

206 statistical analysis of terrace surface points extracted from high resolution LiDAR
207 digital elevation models revealed upstream diverging patterns in the highest terraces,
208 and downstream diverging to parallel patterns in the intermediate and lowest terrace
209 levels (Figure 2; Rodríguez-Rodríguez et al., 2020).

210 **3. Methodology**

211 The cosmogenic nuclide dating technique applied to sediment landforms relies on
212 the measurement of various cosmogenic nuclides produced and stored inside the lattice
213 of a target mineral by the interactions with the cosmic rays (Gosse and Phillips, 2001).
214 The pair of cosmogenic nuclides most frequently used to study alluvial landforms is
215 ^{10}Be - ^{26}Al , as they are produced in the same target mineral (quartz) at a ratio of ~ 6.75
216 largely independent from altitude and latitude (Dunai, 2010). Once sediments are buried
217 deep enough to be fully shielded from cosmic radiation, their initial concentrations start
218 to decay at a pace of $4.9975 \times 10^{-7} \text{ a}^{-1}$ for ^{10}Be (Chmeleff et al., 2010) and $9.83 \times 10^{-7} \text{ a}^{-1}$
219 for ^{26}Al (Nishiizumi, 2004). If sediments have been sufficiently exposed before being
220 buried, the residual concentration of paired ^{10}Be - ^{26}Al cosmogenic nuclides measured in
221 deep samples can be used to solve for the burial time (Granger and Muzikar, 2001).

222 In this study, the timing of river incision and fluvial terrace formation was
223 constrained through the CSEB model proposed by Rodés et al. (2014), which considers
224 the possible occurrence of complex exposure-burial histories before the final deposition
225 of sediments takes place. It is expressed as function of: (i) the apparent pre-depositional
226 average exhumation rate at the catchment source area; (ii) the apparent pre-depositional
227 burial time; (iii) the local denudation rate; and (iv) the terrace surface age.

228 Exhumation rates are considered apparent because, although most reworking
229 processes change the ^{10}Be - ^{26}Al signature towards concentrations that suggest lower
230 erosion rates, there could be scenarios where sediments have been recycled after a long
231 period of burial and, hence, the ^{10}Be - ^{26}Al signature would solely reflect the last erosion
232 rate. In any case, the ^{10}Be - ^{26}Al signatures shall reflect an apparent erosion rate and an
233 apparent burial duration, both corresponding to an unbalanced average of all erosion
234 stages occurred and their respective durations.

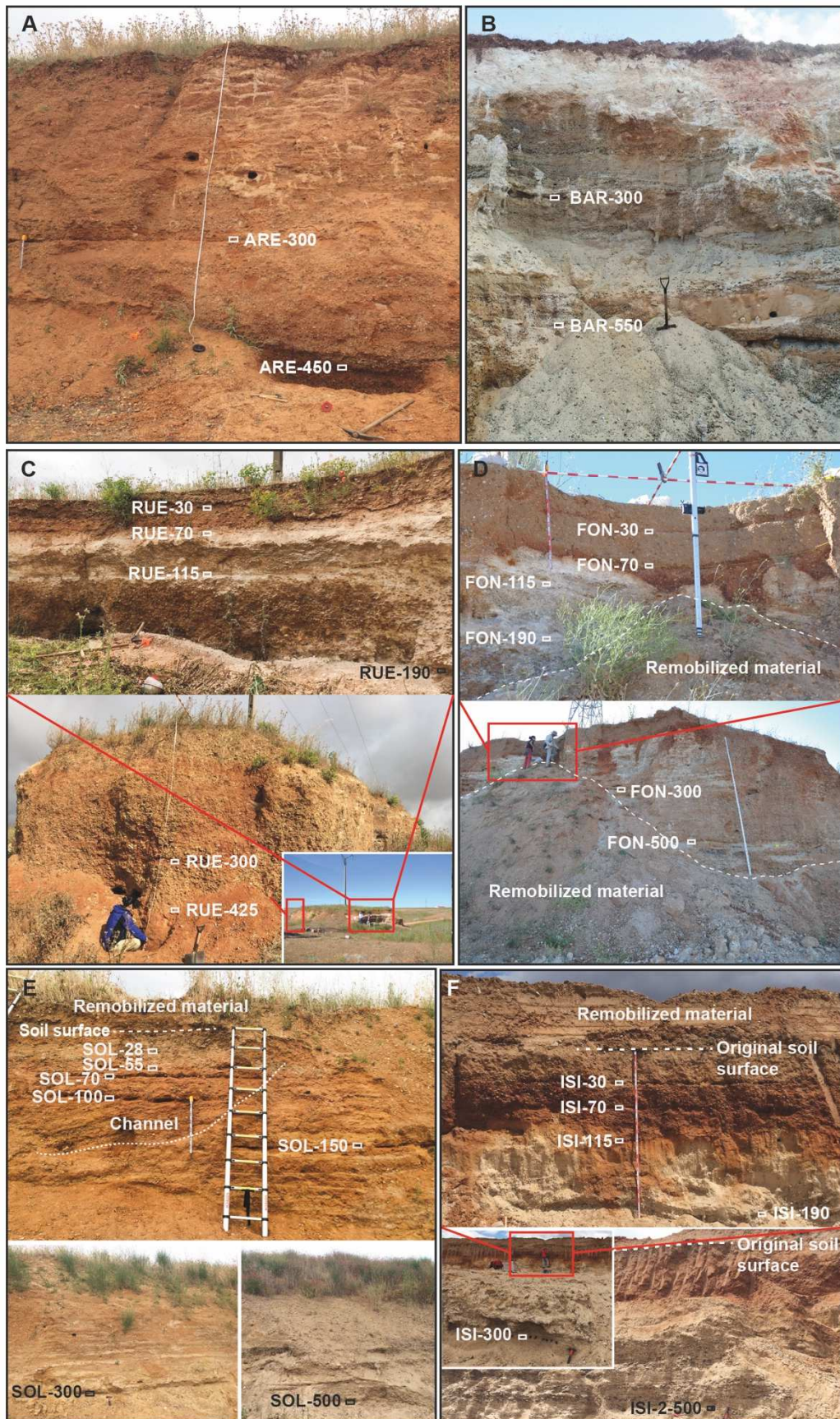
235 *3.1. Terrace depth profile sampling*

236 In order to constrain as much as possible the age of the Duero river terrace staircase,
237 the thickest terrace sequences, displaying well-preserved top surfaces, were
238 preferentially targeted for deep profile sampling. We tried to cover the greatest number
239 of terrace levels distributed over the central CDB, across sections 1, 2, and 3 (located

240 ca. 30-80 km eastward from the WCB; Figure 2). Potential terrace sections were located
241 using high-resolution LiDAR digital elevation models and aerial imagery
242 (<https://www.cnig.es>; last access on June 2016), and visited in the field to verify that
243 sediment thickness was greater than 4 m. Paired ^{10}Be – ^{26}Al cosmogenic nuclides depth
244 profiles were sampled from sections of six fluvial terraces of the Duero river staircase,
245 including a total number of 31 sediment samples taken mostly from sections at open
246 cast quarries dedicated to gravel extraction (named Arentis, Barbado Martín, Foncantín,
247 Jose Isidro Torres, and Sola e Hijos). The following terrace levels were sampled
248 (Figures 2 and 3): T2 (code ARE; 2 samples), T3 (code BAR; 3 samples), T6 (code
249 RUE; 6 samples), T10 (code FON; 6 samples), T11 (code SOL; 7 samples), and T12
250 (code ISI; 6 samples). We collected 6–7 sediment samples per terrace profile
251 exponentially spaced from 20–30 cm below the surface down to 4.25–5 m (Figure 4 and
252 Table I). In the oldest terraces (T2 and T3), the probability of finding saturated profiles
253 was considered to be high and, hence, only the deepest samples of the profile (at 3 and
254 4.50–5.50 m depth, respectively) were taken. The geographic location and altitude of
255 each sampling site was determined in the field by GPS positioning. The maximum
256 surface lowering of sampled terrace remnants was inferred using topographic sections
257 passing through each sampling site, assuming that terrace top surfaces were originally
258 flat. For this purpose, a 3 m cell-size resolution digital elevation model derived from the
259 LiDAR datasets from the Spanish National Institute of Geography was used. Fluvial
260 sediment facies were described at each sampling location. A description of the main soil
261 characteristics (number of horizons, thickness, presence of pedogenic calcrete) is also
262 provided to address age interpretations (in terms of possible hiatuses during terrace
263 aggradation), and to offer an alternative surface lowering scenario for the sampled
264 terraces. Regarding the grain size fraction sampled, given that fluvial deposits in this
265 area are cobble- and pebble-dominated, the pebble fraction in the range 2 mm–2 cm in
266 diameter was targeted in all cases, ensuring that more than 200 particles per sample
267 were collected.

268 Density values assigned to fluvial sediments might have a strong impact in the final
269 age model (Rodés et al., 2011). Thus, twenty-three density measurements were
270 performed in the field for the various fluvial terrace materials identified and sampled,
271 obtaining results in the range 1.49–2.31 $\text{g}\cdot\text{cm}^{-3}$, and an average density value of $1.72 \pm$
272 $0.2 \text{ g}\cdot\text{cm}^{-3}$ (further details are provided in the supplementary material). Based on these
273 results, a range of density values of 1.52–1.92 $\text{g}\cdot\text{cm}^{-3}$ has been introduced in the models,

274 which is in good agreement with reference density values provided for dense coarse
 275 granular soils in some engineering manuals (e.g. González de Vallejo, 2002).



276

277 Figure 3.- Terrace sampling sections: A) T2 at Arentis quarry; B) T3 at Barbado Martín quarry; C)
278 T6 at an old extraction area close to Rueda; D) T10 at Foncastin quarry; E) T11 at Sola e Hijos quarry;
279 and F) T12 at Isidro quarry. Labels indicate sampling depths expressed in centimeters.

280 3.2. Sample treatment and AMS measurement of Be and Al ratios

281 Fluvial sediment samples were crushed and sieved at the *Departament de Dinàmica*
282 *de la Terra i de l'Oceà (Universitat de Barcelona)* in order to reduce the grain size to
283 1mm–250 µm in diameter, optimal for doing the chemical processing. Sample treatment
284 was conducted at *Laboratoire National des Nucléides Cosmogéniques (LN2C) – Centre*
285 *Européen de Recherche et d'Enseignement des Géosciences de l'environnement*
286 (CEREGE, Aix-en-Provence). The extraction of magnetic dark mineral grains was done
287 using a Frantz magnetic separator and applying a magnetic field intensity of 1A. Sample
288 cleaning involved carbonate removal with hydrochloric acid and several acid leaching
289 baths with a mixture of hydrochloric and hexafluorosilicic acids. The isolation and
290 purification of quartz was done through four etching bathes with hydrofluoric acid to
291 ensure a full removal of atmospheric ¹⁰Be. Once cleaned, quartz samples (20–30 g)
292 were spiked with ~100 mg of a phenakite carrier solution with a concentration of 3025
293 ± 9 µg·g⁻¹ of ⁹Be before total dissolution in hydrofluoric acid. Samples were aliquoted
294 for the ICP-OES analysis of the natural ²⁷Al concentration in the samples. Given the
295 low natural concentration of ²⁷Al in the samples (mean value of 2.03 ± 0.66 ppm), a
296 volume of 750–2100 mg of a commercial VWR Prolabo spike solution with a ²⁷Al
297 concentration of 981 ± 4.91 µg·g⁻¹ was added to each sample to ensure a final Al
298 sample of ~2 mg. Beryllium and aluminum were separated from the solution by
299 successive column chromatography using anionic (DOWEX 1X8) and cationic
300 (DOWEX 50WX8) resins. The recovered Be and Al solutions were taken to pH ~8.5 to
301 precipitate the hydroxides, that were subsequently washed in slightly basic solutions.
302 After drying the last precipitates in porcelain crucibles, samples were heated in the oven
303 at 800°C during one hour. Resultant BeO and Al₂O₃ precipitates were mixed with
304 niobium and silver powder to perform the AMS measurements at the French AMS
305 National Facility ASTERisques, located at CEREGE (Aix-en-Provence). Beryllium
306 measurements were calibrated against the reference material NIST–SRM4325 [nominal
307 value of (2.79 ± 0.03) ×10⁻¹¹ equivalent to 07KNSTD within rounding error], while
308 aluminum measurements were calibrated against the in-house standard SM-Al-11
309 [nominal value of (7.401 ± 0.064) ×10⁻¹²] (Arnold et al., 2010). The ASTER ²⁶Al
310 standard (the only available ²⁶Al standard cross-calibrated against the primary standards

311 certified by a round-robin exercise) yields a ratio of $(7.554 \pm 0.104) \times 10^{-12}$ when
312 measured against the ^{26}Al KNSTD10650 standard, 2.1% higher than the nominal value
313 (Rixhon et al., 2011). The SM-Al-11/07KNSTD standardization used in this work
314 implies a $^{26}\text{Al}/^{10}\text{Be}$ production ratio of 6.61 ± 0.52 (Braucher et al., 2011), which is in
315 good agreement with the ~ 6.75 ratio broadly accepted in the literature (Dunai, 2010).
316 Reported analytical uncertainty (1σ) includes: (i) an external uncertainty of $\sim 0.5\%$ that
317 accounts for all effects contributing to ASTER's variability (Arnold et al., 2010); (ii) a
318 counting statistics uncertainty of $\sim 3\%$ ($\sim 1,500$ events) related to the cumulative number
319 of ^{10}Be events and $\sim 4\%$ (~ 850 events) related to the number of ^{26}Al events acquired
320 during AMS measurements; and (iii) the uncertainty linked to the chemical blank
321 correction. The reported analytical uncertainty of the aluminum concentrations also
322 accounts for the errors associated with the ICP-OES analysis (model Thermo iCAP
323 5000 Series) carried out at CEREGE. Long-term AMS measurements of procedural
324 blanks yield a background ratio of $(2.4 \pm 1.5) \times 10^{-15}$ for $^{10}\text{Be}/^9\text{Be}$ and $(2.2 \pm 2.0) \times 10^{-15}$
325 for $^{26}\text{Al}/^{27}\text{Al}$ (Bourlès, personal communication). However, the procedural blank in our
326 dataset yielded ratios of 3.13×10^{-14} for $^{10}\text{Be}/^9\text{Be}$ and 8.76×10^{-16} for $^{26}\text{Al}/^{27}\text{Al}$. We
327 verified that the unusually high $^{10}\text{Be}/^9\text{Be}$ ratio observed in the blank responds to a ^{10}Be
328 contamination of the ^{27}Al carrier solution ($\sim 3.507 \times 10^{-12}$ ppm of ^{10}Be) that has been
329 corrected in all samples.

330 Table I.- Location coordinates (in decimal degrees) and terrace top surface elevation at the sampled
331 terrace depth profiles and measured ^{10}Be and ^{26}Al concentrations.

| Terrace level | Sample | Depth (cm) | [Be-10] ($10^3 \text{ at}\cdot\text{g}^{-1}$) | [Al-26] ($10^3 \text{ at}\cdot\text{g}^{-1}$) |
|---|------------|-------------|---|---|
| T2 41.3522, -4.9159 800 m a.s.l. | ARE-300 | 300 ± 3 | 214.7 ± 7 | 462 ± 31 |
| | ARE-450 | 450 ± 2 | 188.5 ± 6.1 | 263 ± 21 |
| T3 41.3660, -4.9792 779 m a.s.l. | BAR-300 | 300 ± 4 | 340 ± 12 | 974 ± 55 |
| | BAR-550 | 550 ± 3 | 246.5 ± 8.2 | 302 ± 22 |
| | BAR-02-550 | 550 ± 2 | 225 ± 7.5 | 312 ± 27 |
| T6 41.4064, -4.9643 753 m a.s.l. | RUE-030 | 30 ± 2 | 3487 ± 69 | 15500 ± 370 |
| | RUE-070 | 70 ± 2 | 1867 ± 52 | 5260 ± 170 |
| | RUE-115 | 115 ± 2 | 1325 ± 31 | 4440 ± 140 |
| | RUE-190 | 190 ± 3 | 691 ± 24 | 2102 ± 75 |
| | RUE-300 | 300 ± 3 | 436 ± 14 | 693 ± 37 |
| | RUE-425 | 425 ± 2 | 461 ± 14 | 990 ± 43 |
| T10 41.4584, -4.9865 707 m a.s.l. | FON-030 | 30 ± 2 | 1824 ± 48 | 8420 ± 260 |
| | FON-070 | 70 ± 2 | 1168 ± 33 | 5500 ± 170 |
| | FON-115 | 115 ± 2 | 874 ± 25 | 4210 ± 140 |
| | FON-190 | 190 ± 2 | 557 ± 17 | 2122 ± 78 |
| | FON-300 | 300 ± 2 | 523 ± 16 | 1717 ± 59 |

| | | | | |
|------------------|------------|---------|-----------|------------|
| | FON-500 | 500 ± 2 | 338 ± 11 | 1187 ± 65 |
| T11 | SOL-028 | 28 ± 2 | 1044 ± 29 | 5580 ± 170 |
| 41.4908, -5.6197 | SOL-055 | 55 ± 2 | 671 ± 21 | 3540 ± 120 |
| 656 m a.s.l. | SOL-070 | 70 ± 2 | 580 ± 19 | 3340 ± 110 |
| | SOL-100 | 100 ± 2 | 612 ± 22 | 3210 ± 110 |
| | SOL-150 | 150 ± 2 | 458 ± 15 | 2090 ± 68 |
| | SOL-300 | 300 ± 2 | 451 ± 15 | 2081 ± 76 |
| | SOL-500 | 500 ± 2 | 368 ± 12 | 1357 ± 46 |
| T12 | ISI-020 | 20 ± 1 | 939 ± 29 | 4070 ± 130 |
| 41.4735, -5.3685 | ISI-040 | 40 ± 1 | 787 ± 26 | 3920 ± 120 |
| 657 m a.s.l. | ISI-070 | 70 ± 2 | 642 ± 21 | 2855 ± 100 |
| | ISI-110 | 110 ± 4 | 446 ± 14 | 1955 ± 69 |
| | ISI-190 | 190 ± 4 | 376 ± 12 | 1314 ± 62 |
| | ISI-300 | 300 ± 5 | 242.3 ± 8 | 736 ± 59 |
| | ISI-02-500 | 500 ± 5 | 261.6 ± 9 | 829 ± 45 |

332

333 3.3.CSEB age model

334 The ^{10}Be and ^{26}Al concentrations measured in the profiles allowed us to model the
335 shape of the theoretical in-situ produced cosmogenic nuclide signature with sample
336 depth since terraces were deposited, and the construction of a chronological framework
337 compatible with the cosmogenic nuclide signature measured. A Monte Carlo simulation
338 of random models distributed in a window of 0–10 Ma was run in MATLAB[®] to find
339 the chi-square values of the models that best fit the concentrations measured in our
340 profiles. Monte Carlo simulations were run until 300 models fitting the 1-sigma
341 confidence interval were found. Chi-squared minimization was performed for the
342 models fitting the 1-sigma confidence interval (Rodés et al., 2014). The *in situ*
343 production rate of cosmogenic ^{10}Be and ^{26}Al at each sampling site was determined
344 considering the constant production rate model of Stone (2000) and apparent attenuation
345 length values calculated from muonic production rate cross-sections generated using the
346 code from the online calculator formerly known as the CRONUS-Earth online
347 calculator v 2.3 (Balco et al., 2008; Table II). Uncertainties related to cosmogenic
348 nuclides half-life and production rate were not included in age calculations, involving
349 that uncertainties reported for burial durations shall be considered as internal
350 uncertainties. The transmission of half-life and production rate uncertainties would
351 impact the exposure ages by 10% or less, which is negligible compared to uncertainties
352 of the obtained exposure ages.

353 A first modeling was performed without imposing geological constraints relative to
354 the preservation degree of the surface. However, as the terrace preservation is a key

355 factor in determining individual terraces ages (onset of terrace surface exposure),
 356 further models were run limiting the maximum lowering of each surface to better
 357 constraint the exposure age of terrace surfaces. Maximum lowering values assumed in
 358 the final CSEB age model are discussed in the results section with regards of soil
 359 evidence and lowering measurements.

360 Table II.- ^{10}Be - ^{26}Al local production rates (P) and attenuation lengths (A) for spallation (sp), slow
 361 muons (sm) and fast muons (fm) according to Stone (2000) and using the code from CRONUS Calc v 2.3
 362 (<https://hess.ess.washington.edu>; Balco et al., 2008). Catchment production rates were estimated using the
 363 average elevation of the source (1300 m) and the same latitude as the sampling sites because the Duero
 364 Basin is E-W trending.

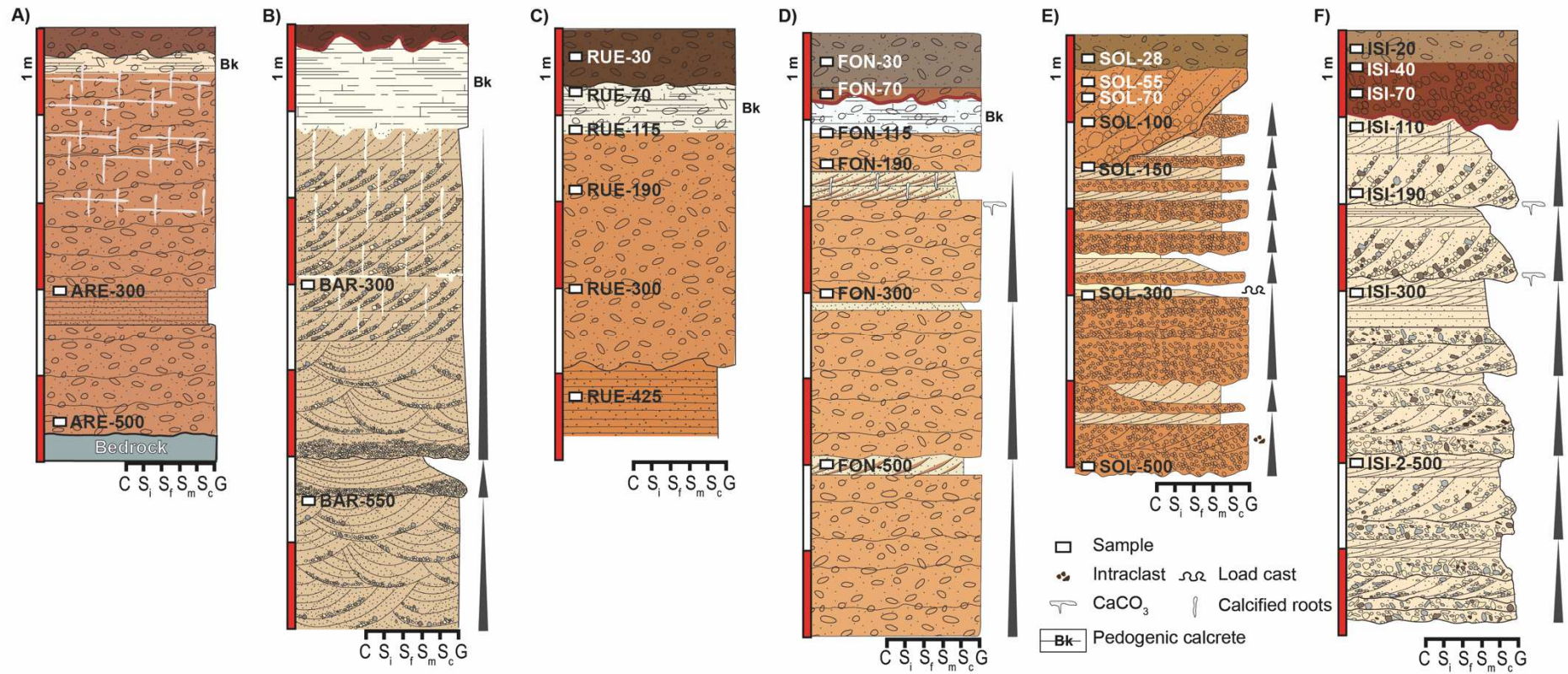
| Location | Isotope | Psp ($\text{at}\cdot\text{g}^{-1}\cdot\text{a}^{-1}$) | Psm ($\text{at}\cdot\text{g}^{-1}\cdot\text{a}^{-1}$) | Pfm ($\text{at}\cdot\text{g}^{-1}\cdot\text{a}^{-1}$) | Asp ($\text{g}\cdot\text{cm}^{-2}$) | Asm ($\text{g}\cdot\text{cm}^{-2}$) | Afm ($\text{g}\cdot\text{cm}^{-2}$) |
|-----------------|------------------|--|--|--|--|--|--|
| Basin source | ^{10}Be | 11.1655 | 0.0663 | 0.0491 | 160 | 859.1591 | 1606.500 |
| | ^{26}Al | 75.3295 | 0.7522 | 0.3381 | 160 | 859.1591 | 1606.500 |
| ARE | ^{10}Be | 7.5358 | 0.0538 | 0.0441 | 160 | 1002.8100 | 1775.0137 |
| | ^{26}Al | 50.8407 | 0.6105 | 0.3042 | 160 | 1002.8100 | 1775.0137 |
| BAR | ^{10}Be | 7.4098 | 0.0534 | 0.0439 | 160 | 1021.5003 | 1819.2790 |
| | ^{26}Al | 49.9910 | 0.6050 | 0.3029 | 160 | 1021.5003 | 1819.2790 |
| RUE | ^{10}Be | 7.2586 | 0.5028 | 0.0437 | 160 | 1016.4472 | 1784.2750 |
| | ^{26}Al | 48.9709 | 0.5983 | 0.0433 | 160 | 1016.4472 | 1784.2750 |
| FON | ^{10}Be | 6.9952 | 0.0517 | 0.0433 | 160 | 1041.6347 | 1830.8945 |
| | ^{26}Al | 47.1941 | 0.5866 | 0.2982 | 160 | 1041.6347 | 1830.8945 |
| SOL | ^{10}Be | 6.7157 | 0.0506 | 0.0428 | 160 | 1060.3815 | 1852.4256 |
| | ^{26}Al | 45.3082 | 0.5740 | 0.2950 | 160 | 1060.3815 | 1852.4256 |
| ISI | ^{10}Be | 6.7175 | 0.0506 | 0.0428 | 160 | 1060.1647 | 1852.1961 |
| | ^{26}Al | 45.3200 | 0.5742 | 0.2950 | 160 | 1060.1647 | 1852.1961 |

365 4. Results

366 4.1. Sampled terrace depth profiles: sedimentology and soil characteristics

367 Terraces T2, T3, T6, and T10 were sampled along cross section 1, located ca. 70-80
 368 km east from the WCB (Figures 4 and 5). Fluvial sediment thickness ranges between
 369 4.2 and 4.7 m in terraces T2 and T6, and reaches up to 7 m in terrace levels T3 and T10
 370 (Figure 4). Fluvial terraces T2 and T3 are lying directly on top of the Miocene bedrock,
 371 which locally consists of grey clay and marls. Fluvial sequences sampled in terraces T2,
 372 T6 and T10 are composed by reddish grain-supported cobble and gravel sediments with
 373 sandy matrix, displaying massive strata or parallel to low-angle bedding, and locally
 374 cobble imbrications. Some few centimeters-thick intercalations of sand with sparse
 375 gravels are also present, showing parallel bedding (T2 and T6) or planar cross-bedding
 376 (T10). These terraces probably represent the stacking of ancient river bars in a braided

377 fluvial system of high flow regime. Meanwhile, the sequence of terrace T3 is richer in
378 sandy intervals compared to T2, T6 and T10. Particularly, T3 is composed by
379 decametric to centimetric sets of sand and gravel sediments showing normal graded
380 stratification, and displaying through cross-bedding close to the base and planar cross
381 bedding towards the top. Thus, sediment architecture in T3 reflects a fluvial system of
382 lower flow energy regime than in terraces T2, T6 and T10.



384

385

386

387

Figure 4.- Stratigraphic sections of the sampled terraces showing the distribution of samples in each terrace profile (grains size key is: C- clay; S_i- silt; S_f- fine sand; S_m- medium sand; S_c- coarse sand; G- gravel): A) T2 at Arentis quarry; B) T3 at Barbado Martín quarry; C) T6 at an old extraction area close to Rueda; D) T10 at Foncastin quarry; E) T11 at Sola e Hijos quarry; and F) T12 at Isidro quarry.

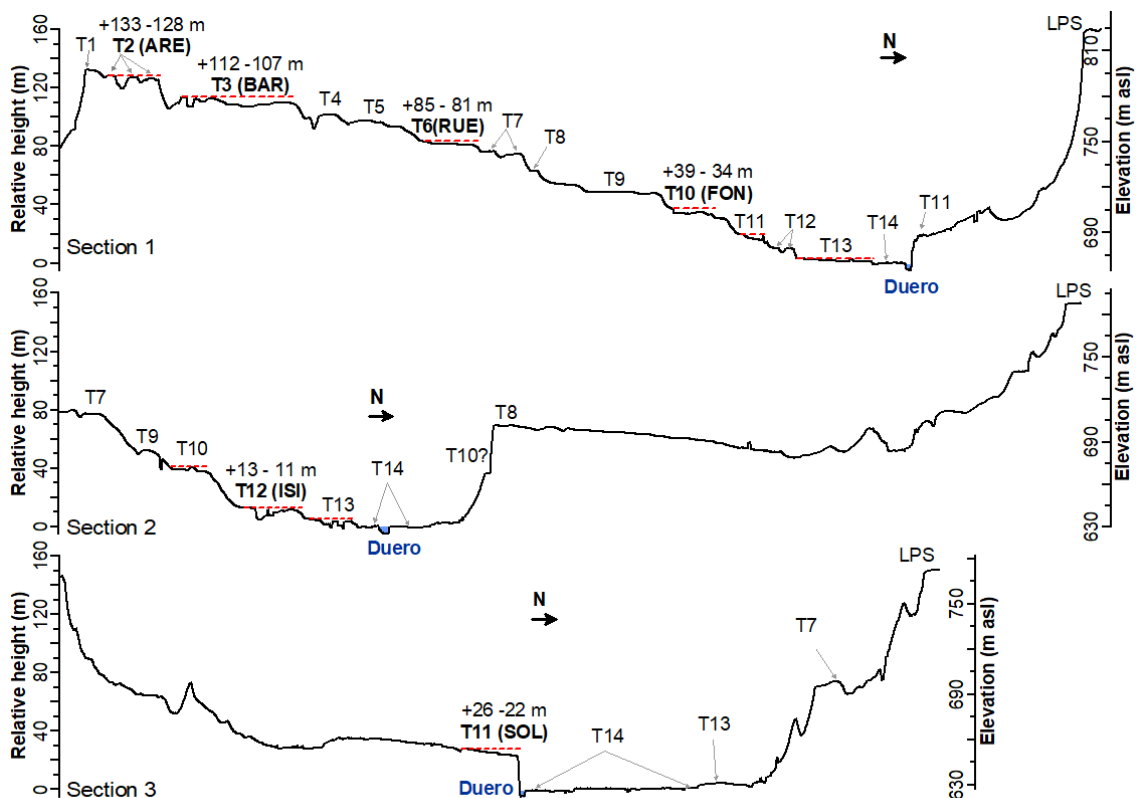
388 The youngest terraces (in terms of relative age) targeted for sediment depth profile
389 sampling are T11 and T12, respectively sampled at cross sections 2 and 3 placed ca. 22
390 and 42 km upstream from the Arribes knickzone (Figures 2 and 5). The sequence of
391 T11 at SOL sampling site is 5.5 m-thick and includes alternations of reddish gravel
392 units and yellowish sand and clay intervals arranged as normal graded sequences
393 (Figure 4). The thickness of gravel units decreases from metric-decametric to
394 centimetric beds upwards, mostly showing massive or parallel stratification and
395 eventually displaying cross-bedding and muddy intraclasts. Gravel units alternate with
396 thinner units of coarse-medium sand that gradually decrease in grain size towards the
397 top to fine sand, silt and clay. Deformation structures such as load casts are visible in
398 the clay intervals. Altogether, they are arranged as stacked normal graded sequences. A
399 channel infill cross-cut the sequence previously described in the uppermost 1.5 m of the
400 profile, composed by cross-bedded cobble and gravel sediments with sandy matrix. We
401 interpret the lowest part of the sequence as the floodplain facies adjacent to the river
402 channel infill. Finally, the youngest terrace level sampled, T12, is ca. 7 m in thickness.
403 It is mostly composed by cross-bedded cobble, gravel and coarse sand sediments
404 arranged as normal graded sequences. The uppermost part of the sequence culminates
405 with coarse to medium sand beds displaying parallel or planar cross-bedding. The
406 fluvial flow regime would be comparable or slightly more energetic than during the
407 formation of T3 considering the grain size and sediment structures identified in the
408 field.

409 Soils in the sampled terraces are generally around 1–1.15 m-thick (T3, T6, T10,
410 T12) independently from their relative age, and exceptionally thinner than 1m in some
411 terraces (0.5 m-thick in T2 and 0.4 m thick in T11; Figure 4) most likely due to post-
412 soil formation erosion. Two similarities were noticed between the soils developed in the
413 sampled terraces. First, the presence of an argillic horizon with intense dark red
414 coloring, which is directly exposed to the surface in the oldest terraces T2 and T3, or at
415 the base of a dark-brown argillic horizon (horizon B) in the intermediate (T6) and low
416 terraces (T10 and T12). Second, the occurrence of a well-developed petrocalcic horizon
417 (cemented by calcium carbonate) below the dark red argillic horizon in terraces T2 (20
418 cm-thick), T3 (100 cm-thick), T6 (50 cm-thick), and T10 (40 cm-thick), starting at
419 depths of 30-20 cm in the highest terraces (T2-T3) and at 70 cm in T6 and T10 (Figure
420 4 A-D). It is worth mentioning that these two features are missing in the soil profile at
421 the sampling site of T11, where the soil shows a brown argillic horizon B ca. 40 cm-

422 thick. Previous studies have classified the soils in the study area as Alfisols (Pérez-
 423 González, 1982). More specifically they could correspond to Xeralfs, which are typical
 424 of Mediterranean-type climate regimes and usually remain dry for extended periods in
 425 summer (Soil Survey Staff, 2015).

426 *4.2. Terrace surface preservation and maximum lowering estimates*

427 Across Duero valley profiles passing through the sampling sites show the vertical
 428 height of terrace scarps between successive levels (Figure 5). Although their top
 429 surfaces are relatively well preserved in the study area, they show evidence of runoff
 430 erosion and deflation (like blowout depressions up to 2 m deep and ventifacts),
 431 indicating that erosion was locally important. Moreover, terraces might be prone to
 432 burial by slope deposits and tributary fans from adjacent terrace levels (Mather et al.,
 433 2017), but this is not an issue at our particular sampling sites. In order to constrain the
 434 exposure age of terrace surfaces in the CSEB model, we limit the maximum lowering
 435 experienced by each surface based on geological evidence.



436
 437 Figure 5.- Sections of the Duero river crossing the sampling sites (see Figure 2 for the exact location of
 438 each section). They show the full sequence of terrace levels preserved in each area and the spatial
 439 relationships between them and with the modern floodplain (reference level to calculate the relative
 440 height) and the LPS erosional surface to the North. Red dashed lines indicate the possible position of
 441 original terrace top surfaces, providing a minimum estimate for the post-depositional maximum lowering
 442 of the surface.

443 A first estimate of the true maximum lowering values of the sampled surfaces was
444 done measuring the altitude difference between the terrace top surface at the sampling
445 point and the maximum altitude observed in the surrounding areas of the same terrace
446 outcrop. Assuming that the original terrace surface was flat (represented by red dashed
447 lines in Figure 5), total lowering estimates up to ~5 m for T2 (ARE), ~3.5 m for T3
448 (BAR), ~3 m for T6 (RUE) and T10 (FON), ~4 m for T11 (SOL), and ~1.5 m for T12
449 (ISI) were inferred. Additional lowering linked to the erosion of the highest portion of a
450 terrace top surface is difficult to infer due to the lack of indicators. However, since
451 evidence of fill terraces was not found at the studied sites, denudation would be limited
452 to the height difference between the highest sectors of a terrace top surface and the base
453 of an immediately higher terrace. Therefore, no more than ~3 m of additional erosion
454 would be possible in terrace T2 (ARE), ~15 m for terrace T3 (BAR), ~7 m for terrace
455 T6 (RUE), ~8-6 for terrace T10 (FON), and ~5 m for terrace T12 (ISI). In the case of
456 terrace T11 (SOL), the lack of higher terrace levels at Villalazán section makes
457 impossible a direct measurement, but long profile analysis based on terrace levels
458 preserved in the area shows an increasing trend in height difference between terrace
459 levels T10 and T11 towards the WCB, placing the corresponding terrace scarp between
460 ~15–10 m (Rodríguez-Rodríguez et al., 2020). Considering that the maximum thickness
461 of fluvial sediments observed for terrace T10 is 7 m, a total lowering in the range ~8–3
462 m can be inferred for T11 (SOL).

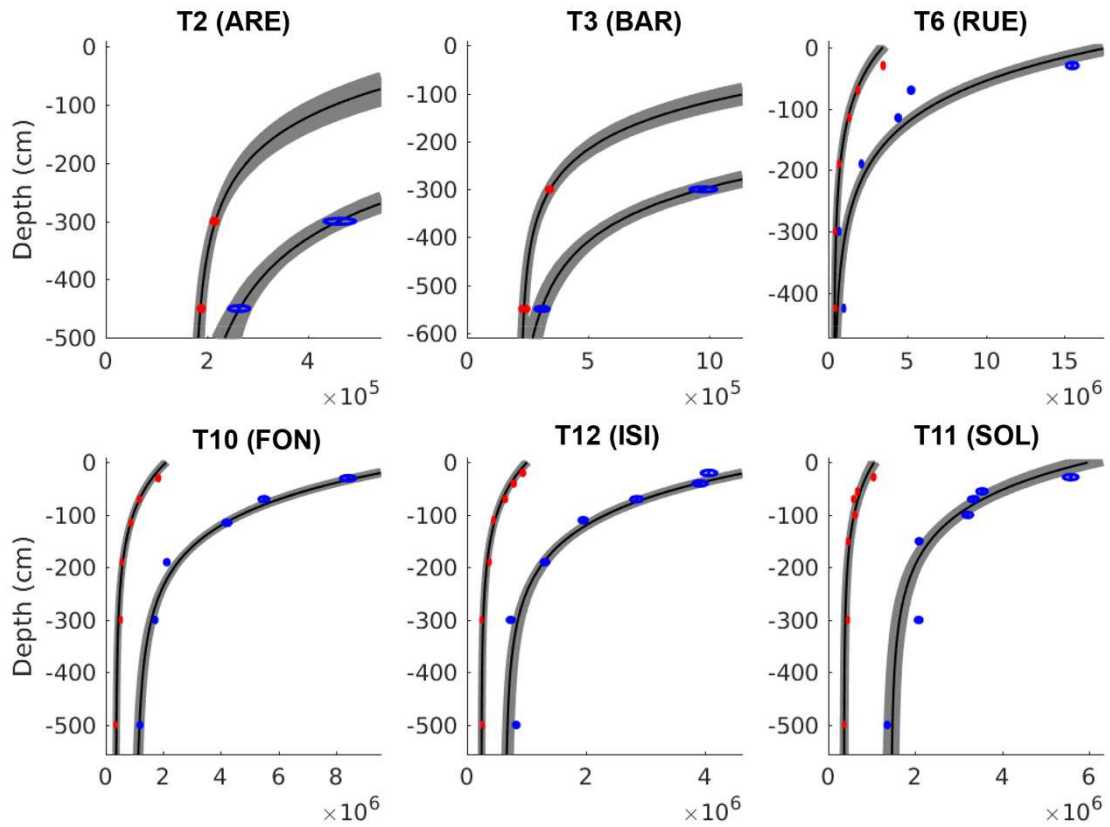
463 An alternative scenario of surface lowering was inferred from the soil characteristics
464 observed in the different terraces (number and thickness of horizons preserved, presence
465 of pedogenic carbonates). Terraces T2 to T10 contain pedogenic calcrete horizons (Bk),
466 reaching ~0.2 m in thickness in T2 (ARE), ~1 m in T3 (BAR), and ~0.4-0.5 m in T6
467 (RUE) and T10 (FON). Pedogenic calcrete formation might follow different paths
468 depending on the local interplay between erosion, deposition and diagenesis (Alonso-
469 Zarza, 2003), occasionally leading to the aerial exposure of the calcrete horizon if
470 erosion overcomes local sedimentation (which is not observed in the studied terraces).
471 As all are soils developed from similar parental materials and in an area of
472 homogeneous climate conditions, assuming a zero-erosion scenario it would be
473 expected that the thickness of the Bk horizon would decrease according to the relative
474 age sequence because the oldest terraces have had more time to developed and have
475 experienced the same climatic variations as those developed at lower levels in the

476 staircase. For instance, the Bk horizon in terrace T2 (ARE) should be at least 0.8 m
477 thicker than it actually is to be similar to that preserved in terrace T3 (closest level
478 placed right below T2). Regarding the location of the Bk horizon in the soils, the upper
479 depth of the Bk horizon in the different terraces is found at ~0.3 m in T2 (ARE), ~0.2 m
480 in T3 (BAR), and ~0.7 m in T6 (RUE) and T10 (FON). Taking as reference both the
481 thickness and the depth of the upper Bk horizon's top in terraces T6 and T10, which
482 show identical values, the oldest terraces T2 and T3 would have experienced a total
483 surface lowering of 1.2 m and 0.5 m respectively. The lowest terraces T11 (SOL) and
484 T12 (ISI) lack a Bk horizon and, hence, the single criteria available are the number and
485 thickness of horizons preserved in the youngest terrace T12. The soil in terrace T12
486 (ISI) is ~40 cm thicker and better developed (up to three well distinguished horizons)
487 than the soil developed in terrace T11 (SOL) providing a minimum lowering estimate
488 for the latest. Finally, for terraces T6, T10 and T12, a total surface lowering value of 0.2
489 m has been arbitrarily assumed to avoid an unrealistic null value. The soil-based
490 scenario simplifies factors involved in soil formation (especially at local level, which
491 hampers a soil-based lowering estimation with confidence), but it offers an alternative
492 scenario where total surface lowering since terrace abandonment is minimal instead of
493 zero. The two lowering scenarios showcase well how this parameter affects exposure
494 age interpretation.

495 4.3. Age model results

496 The ^{10}Be - ^{26}Al concentrations measured in six depth profiles were used to obtain
497 multiple CSEB models for the Duero river terraces (Figure 6) considering different
498 maximum lowering scenarios (Table III). Exposure ages for terraces T3 to T12 would
499 range between 2.5 and 0.14 Ma when no constraint on maximum lowering is applied
500 (only the morpho-stratigraphic order of the terraces was considered; Figure 7). If the
501 maximum lowering is constrained based on geomorphological interpretations and
502 measurements made in topographic sections, resultant exposure ages for the
503 investigated terraces would be: 2265 to 265 ka for T3; 2210 to 478 ka for T6; 1078 to
504 554 ka for T10; 549 to 117 ka for T11; and 217 to 150 ka for T12. However, exposures
505 ages would be considerably younger when total surface lowering is estimated based on
506 soil characteristics. Assuming a scenario of minimum total surface lowering (up to 0.2
507 m) for terraces showing well-preserved soils and additional lowering increases for other
508 terraces based on soil observations previously discussed, we obtained: 997 to 284 ka for
509 T3; 611 to 449 ka for T6; 325 to 248 ka for T10; 171 to 100 ka for T11; and 142 to

510 115 ka for T12. The lack of degrees of freedom in the ^{10}Be - ^{26}Al model of terrace T2
 511 prevents the calculation of the surface exposure age uncertainty, and hence, results
 512 displayed in Table III for the two lowering scenarios proposed would only constitute a
 513 minimum estimate.

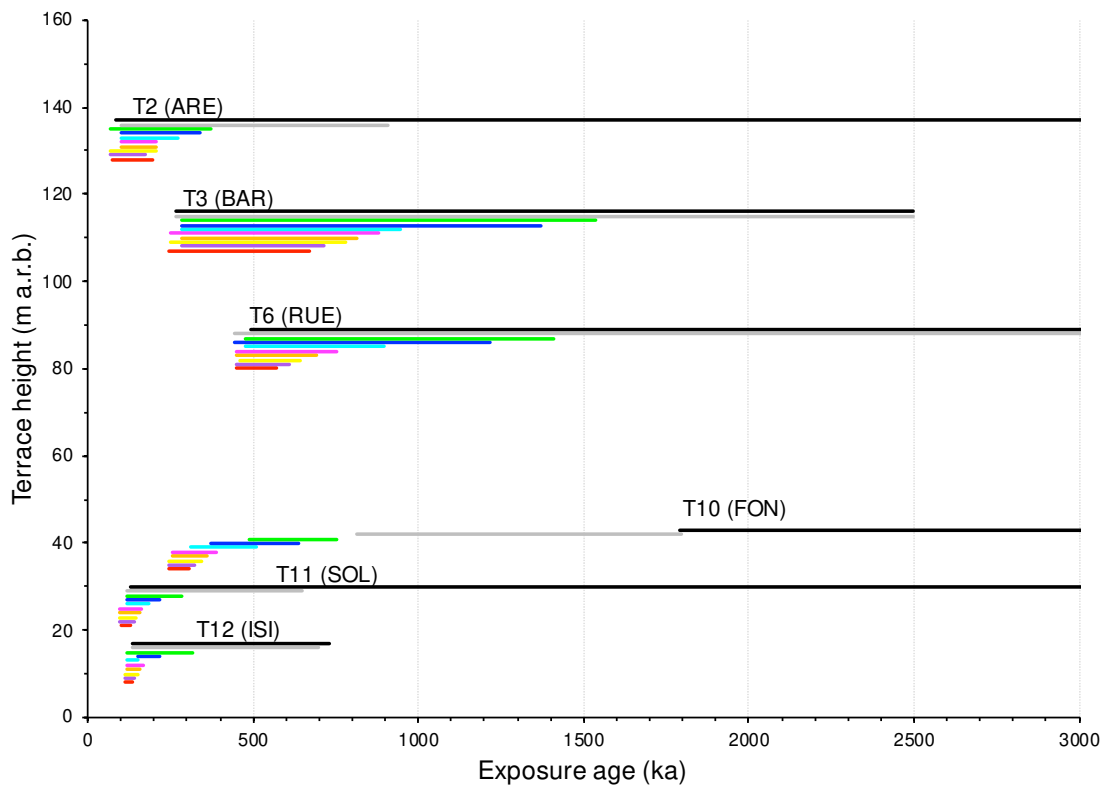


514

515 Figure 6.- Best fitting CSEB models (black lines) fitting the ^{10}Be and ^{26}Al concentrations (red and
 516 blue ellipses) and CSEB models fitting the data within one-sigma confidence level (grey lines).

517 Table III.- CSEB dating age models of fluvial terraces sampled upstream from the WCB (sampling
 518 locations are shown in Figure 2) considering three different scenarios of maximum lowering: free
 519 (lowering limited to 100 m); maximum total lowering estimated from surface preservation; and maximum
 520 lowering estimated from soil characteristics. Due to the lack of degrees of freedom in profile adjustment,
 521 the exposure ages provided for T2 must be considered only minimum estimates.

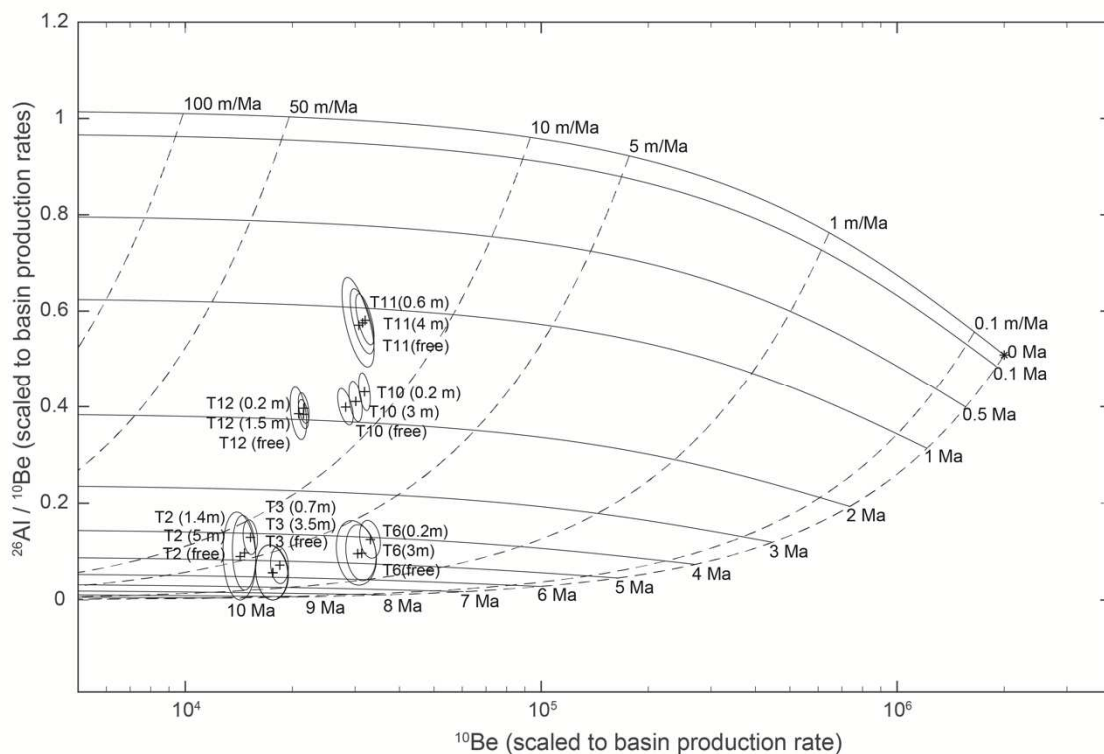
| Terrace (lowering) | Relative height (m) | ¹⁰ Be inherited (10 ⁴ at.g ⁻¹) | ²⁶ Al inherited (10 ⁴ at.g ⁻¹) | Basin denudation rate (m.Ma ⁻¹) | Exposure age (Ma) | Burial duration (Ma) | In situ denudation rate (m/Ma) |
|-----------------------|------------------------|---|---|--|----------------------|----------------------------|---|
| T2 (free) | +133-128 | 14.4-17.8 | 0-19.6 | 0-6.3 | 0.08-∞ | 3.67-10.10 | <16.8 |
| T3 (free) | +112-107 | 17.8-21.9 | 0-15.1 | 0-3.4 | 0.27-2.50 | 4.50-9.66 | <4.4 |
| T6 (free) | +85-81 | 30.0-38.9 | 7.2-37.5 | 0-3.1 | 0.50-∞ | 3.55-7.88 | <1.6 |
| T10 (free) | +39-34 | 30.3-33.5 | 79.3-93.1 | 8.0-10.7 | 1.79-∞ | 1.67-1.97 | 2.7-3.3 |
| T11 (free) | +26-22 | 31.2-38.4 | 117.7-151.3 | 9.7-14.1 | 0.13-∞ | 0.94-1.39 | 0.5-8.7 |
| T12 (free) | +13-11 | 22.3-24.8 | 53.4-69.5 | 10.4-12.7 | 0.14-0.73 | 1.72-2.15 | <6.9 |
| T2 (5 m) | +133-128 | 15.3-17.8 | 2.3-19.5 | 0.8-6.3 | 0.10-0.91 | 3.67-7.41 | <15.1 |
| T3 (3.5 m) | +112-107 | 17.8-22.0 | 0-15.2 | 0-3.4 | 0.27-2.27 | 4.48-9.67 | <3.9 |
| T6 (3 m) | +85-81 | 31.9-38.8 | 9.6-36.8 | 0.6-2.6 | 0.48-2.21 | 3.80-6.09 | <1.6 |
| T10 (3 m) | +39-34 | 32.6-35.5 | 85.8-103.6 | 7.6-9.5 | 0.55-1.08 | 1.65-1.94 | 2.7-3.3 |
| T11 (4 m) | +26-22 | 32.9-38.4 | 126.7-151.2 | 9.7-13.4 | 0.12-0.55 | 0.92-1.34 | <8.4 |
| T12 (1.5 m) | +13-11 | 23.5-25.1 | 58.7-67.7 | 10.4-12.9 | 0.15-0.22 | 1.73-2.10 | 0.6-5.6 |
| T2 (1.4 m) | +133-128 | 16.4-18.0 | 11.0-19.2 | 3.7-6.2 | 0.10-0.38 | 3.70-4.70 | <9.9 |
| T3 (0.7 m) | +112-107 | 19.6-22.0 | 4.8-15.5 | 1-3.3 | 0.28-0.98 | 4.47-6.53 | <1.8 |
| T6 (0.2 m) | +85-81 | 34.9-39.9 | 22.0-41.3 | 1.3-3.1 | 0.45-0.61 | 3.53-4.80 | <0.4 |
| T10 (0.2 m) | +39-34 | 34.7-37.4 | 96.3-114.1 | 7.7-9.4 | 0.25-0.33 | 1.54-1.83 | <0.7 |
| T11 (0.6 m) | +26-22 | 34.1-38.4 | 132.8-152.4 | 9.7-13.2 | 0.10-0.17 | 0.91-1.31 | <4.2 |
| T12 (0.2 m) | +13-11 | 23.5-25.2 | 60.7-70.1 | 10.5-12.6 | 0.12-0.14 | 1.74-2.03 | <1.6 |



522
 523 Figure 7.- Exposure ages of CSEB models fitting the data with no restrictions (black) and with limited
 524 maximum total lowering of the terrace surfaces by 5 m (grey), 2 m (green), 1.5 m (blue), 1 m (cyan), 0.5

525 m (magenta), 0.4 m (orange), 0.3 m (yellow), 0.2 m (violet), and 0.1 m (red). Without lowering limitation
 526 based on local evidence, the exposure age of most terraces (T3 to T12) is limited to 2.5 Ma based on the
 527 maximum exposure age of T3 (ARE).

528 Burial durations reported for the studied terraces cover the time interval 0.9 to 2.0
 529 Ma for terraces T10 (FON), T11(SOL) and T12 (ISI), while those found in the highest
 530 terraces T6 (RUE), T3 (BAR) and T2 (ARE) cover a longer time interval of 3.5 to 9.6
 531 Ma, evidencing longer transport times and complex exposure histories for the highest
 532 terraces (Figure 8). Modelled basin denudation rates coetaneous to the oldest terrace
 533 levels were much lower (up to 3–6 m·Ma⁻¹) than those found (7.7–13.4 m·Ma⁻¹) in the
 534 youngest terraces.



535
 536 Figure 8.- Inherited concentrations from table III plotted over a “banana plot” generated using the
 537 average basin production rates, following Lal & Arnold (1985). The mountain ranges that limit the
 538 Cenozoic Duero Basin worked as source area of sediments, located at a mean elevation of 1300 m
 539 (estimation based on a 25 m resolution DEM from the Spanish National Institute of Geography).
 540 Therefore, all ¹⁰Be and ²⁶Al concentrations in this figure are scaled to surface production rates of 11.3 and
 541 76.5 at·g⁻¹·a⁻¹ respectively. This model allows us to classify the origin of these sediments in two groups:
 542 an old group of sediments found in T2, T3 and T6 generated c. 5 Ma ago at a stable landscape (apparent
 543 denudation rate < 10 m·Ma⁻¹); and a young group of sediments found at T10, T11 and T12 generated 2–1
 544 Ma ago at an active landscape (apparent denudation rate > 10 m·Ma⁻¹).

545 5. Discussion

546 5.1. Pattern of erosion at basin scale and timing of basin opening

547 Calculated exposure time using the CSEB model of Rodés et al. (2014) combined
 548 with the terrace staircase configuration (which indicates the relative age sequence)
 549 provides a time reference for the starting point of incision and terrace formation as a

550 landform within the landscape (abandonment age). The abandonment age is limited to
551 ca. 2.27–0.55 Ma in terrace T3 (+112–107 m), ca. 2.21–0.55 Ma in terrace T6 (+85–81
552 m), ca. 1.08–0.55 Ma in terrace T10 (+39–34 m), 0.55–0.15 Ma in terrace T11 (+26–22
553 m), and 0.22–0.15 Ma in terrace T12 (+13–11 m) for a lowering scenario constrained
554 based on terrace topography and considering the relative age sequence (helps in
555 narrowing the mathematical solutions of the CSEB model incompatible with the
556 staircase configuration). Thus, terraces T3 to T6 would be ascribable to the Early
557 Pleistocene, T10 to the Early-Middle Pleistocene and terraces T11 and T12 to the
558 Middle Pleistocene. In contrast, the abandonment age is limited to ca. 0.98–0.45 Ma in
559 terrace T3 (+112–107 m), ca. 0.61–0.45 Ma in terrace T6 (+85–81 m), ca. 0.33–0.25 Ma
560 in terrace T10 (+39–34 m), 0.17–0.12 Ma in terrace T11 (+26–22 m), and 0.14–0.12 Ma
561 in terrace T12 (+13–11 m) for a lowering scenario constrained based on soil
562 characteristics, ascribing terraces T3 to T6 to the Early-Middle Pleistocene, terrace T10
563 to the Middle Pleistocene, and terraces T11 and T12 to the Middle-Upper Pleistocene.
564 Both scenarios provide an estimate for the timing of floodplain abandonment and
565 terrace formation due to river incision that seem to be in agreement with previous
566 interpretations, based on other techniques (OSL/TL, AAR, ESR and palaeomagnetic
567 chronologies), which ascribed the full terrace staircase to the Pleistocene (Silva et al.,
568 2017). They are also consistent with previous interpretations based on erosional
569 surfaces developed on top of the Neogene infill sediments at the CDB. Close to the
570 Iberian Chain, the top surface of the UPL shows karstification evidence that has been
571 ascribed to the Late Miocene-Early Pliocene, due to a sedimentation break before the
572 onset of the Neogene basin emptying (Benito-Calvo and Pérez-González, 2007). A
573 second erosional surface (LPS) was formed at a lower elevation, on top of the LPL
574 (Figure 2), which connects with the top surface of alluvial fans close to the source area
575 of sediments in the Iberian Chain (Benito-Calvo and Pérez-González 2007). According
576 to these authors, the LPS was formed prior to Pleistocene fluvial incision and could be
577 considered Pliocene or Plio-Pleistocene. Thereafter, the highest terraces linked to the
578 Duero river (T1, T2 and T3) were formed upstream from the Duero knickzone in the
579 Early Pleistocene, starting at T1, the uppermost terrace preserved (+135–131 m respect
580 the modern floodplain), which locates several tens of meters below the LPS (Figure 2).
581 If the soil-based lowering scenario is considered, the ages obtained for the lowest
582 terraces in our study area (hanging at +39 and +13 m) yield comparable depositional
583 ages to those obtained through OSL by Cunha et al. (2019) in the DLR, which are

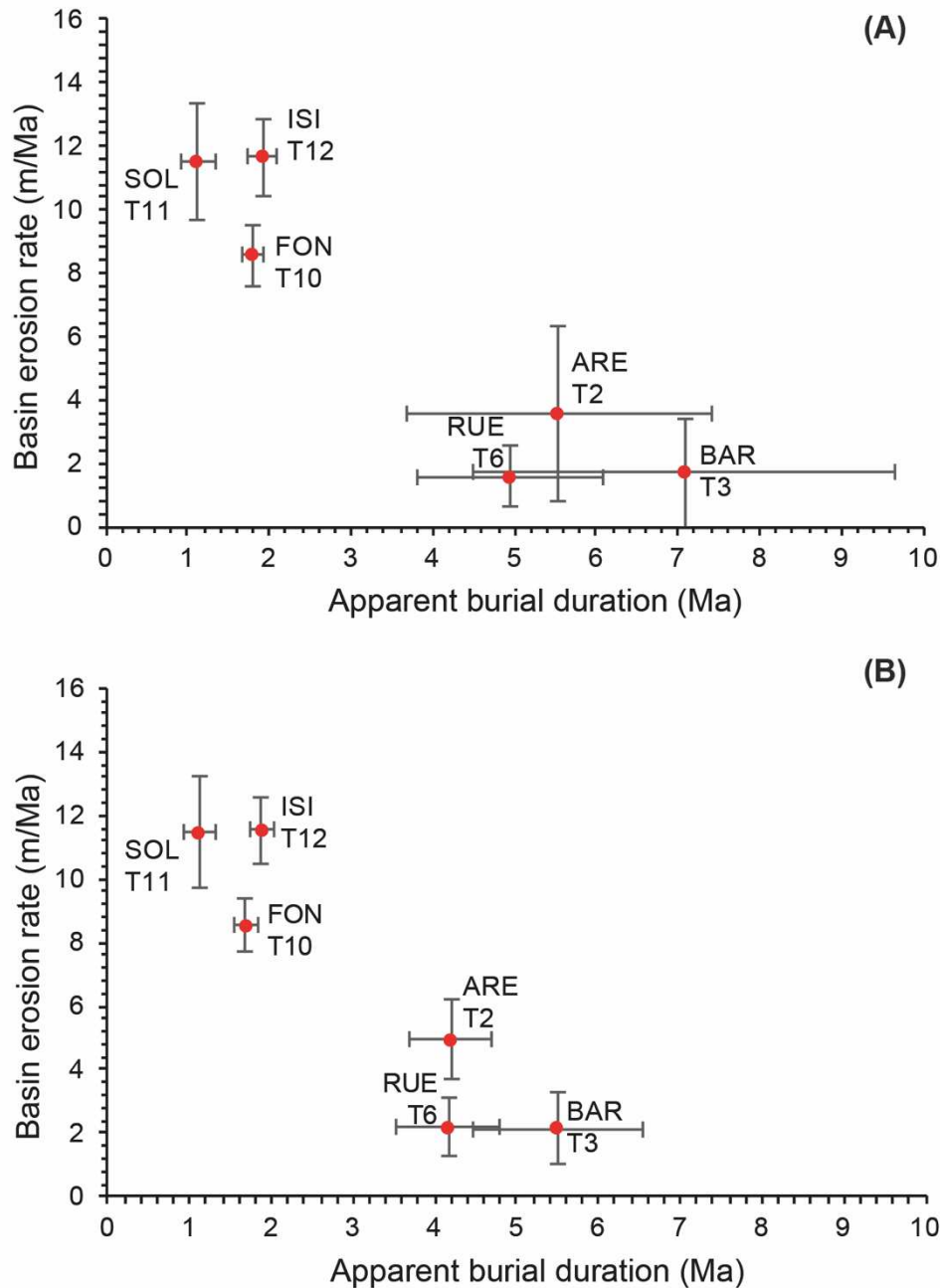
584 hanging between +53 and +13 m above the river bed between Pocinho and Barca
585 d'Alva (ca. 360–12 ka). In contrast, the lowest terraces at the DLR are remarkably
586 younger than the lowest terraces in the CDB when the lowering scenario based on
587 terrace surface topography is considered. In any case, the DLR terraces are located
588 downstream the Arribes knickzone at 200 m a.s.l. (500 m below the terrace staircase
589 studied here), and point to several stages of terrace formation in a different stretch of the
590 Duero long profile placed between the Duero lower and upper reaches (DLR and CDB
591 respectively; Figure 1).

592 The inherited cosmogenic nuclides in a depth profile represent the signature of the
593 sediment at the time of its deposition. In a simple burial history, sediments are eroded
594 from the source area and deposited in a river terrace carrying an inherited cosmogenic
595 signature that is proportional to the average exhumation rate at the source area and the
596 travel time until being buried. However, more complex histories with multiple
597 exhumation/burial episodes before the final burial event are also possible. Presumably,
598 sediments found in the Duero terrace depth profiles come from a diverse source area
599 located at the basin periphery, the highlands of the Cantabrian Mountains to the North,
600 the Iberian Chain to the East and the Sistema Central to the South. Moreover, sediments
601 eroded from the source area might have been mixed with recycled sediments from the
602 Duero Cenozoic Basin, resulting in a material with mixed signature. Thus, inheritance-
603 derived ages and basin erosion rates might inform on the evolution of the basin's
604 bedrock denudation through time, while apparent burial durations may provide an
605 estimate for the maximum travel time of sediments from the source area to the terrace in
606 which they were found. These are key factors potentially related to the landscape
607 response to exorheism.

608 Apparent burial durations calculated from the inherited ^{10}Be and ^{26}Al
609 concentrations in the highest terraces (T2, T3 and T6) indicate maximum sediment
610 travel times in the range 3.5 to 9.7 Ma, while those found in the lowest terraces (T10,
611 T11 and T12) yield values between 0.9 and 2.2 Ma (Figure 9). The several million-years
612 difference between the maxima and minima values reported for the highest terraces is
613 compatible with higher proportions of recycled sediments with inherited ^{10}Be – ^{26}Al
614 concentrations. Also, apparent burial durations in the older terraces seem to be in
615 reverse stratigraphic order, suggesting that the river was eroding a basin filled with
616 sediments from top (younger sediments) to bottom (older sediments) when sediments
617 included in T2 and T3 were formed (>3.5 Ma). Average denudation in the basin source

618 remained relatively low ($<3\text{-}6\text{ m}\cdot\text{Ma}^{-1}$), suggesting that these palaeo-sediments were
619 generated in a stable and relatively inactive basin.

620 Sediments included in the lowest terraces (T10, T11 and T12) indicate that average
621 denudation rates at basin scale were already doubled ($7.7\text{-}13.4\text{ m}\cdot\text{Ma}^{-1}$) $\sim 2\text{-}1\text{ Ma}$ ago.
622 The lower proportion of inherited sediments and the acceleration of denudation rates at
623 basin scale are both reflecting that sediments included in the lowest terraces contain a
624 higher proportion of fresh sediments eroded from bedrock than those found in the
625 highest terraces (Figure 9). A moderate mixed origin of sediments is then assumed for
626 the lowest terraces possibly generated as the upper Duero River started to cut through
627 bedrock materials under much more erosive conditions, with basin average denudation
628 rates comparable to those found in other exorheic basins across Europe (e.g. Schaller et
629 al., 2016a).



630

631 Figure 9.- Apparent basin denudation rates in the catchment area (y-axis) and apparent burial durations
 632 (x-axis) are both calculated from inherited ^{10}Be – ^{26}Al concentrations measured in the terrace depth
 633 profiles. They are both representative for the Duero Basin evolution and the exposure history of sediment
 634 particles until being deposited in the studied terraces: (A) maximum lowering constrained based on
 635 terrace surface topography and (B) maximum lowering constrained based on soil characteristics. In both
 636 lowering scenarios, the highest terraces indicate lower basin denudation rates and older apparent burial
 637 durations than in the lowest terraces, reflecting a considerable acceleration of incision along the upper
 638 Duero river around 2 Ma, already in response to the basin opening to the Atlantic Ocean.

639

The opening of a closed basin involves a change in the long profile of the drainage
 640 network as the incision wave migrates upstream from the opening point. The
 641 acceleration of the basin denudation rates around ca. 4–2 Ma, and the marked

642 differences in the inherited signatures of the terrace deposits, evidence a timing delay
643 between the basin opening and the arrival of the retrogressive erosive wave, nucleated
644 at the opening zone, to the source area of sediments. This delay supports the hypothesis
645 of the two trains of knickpoint waves traveling at different speeds through the soft
646 Neogene sediment cover and the hard-Paleozoic bedrock (Struth et al., 2019). Hence,
647 the low-propagating knickpoint wave travelling through the more resistant Paleozoic
648 bedrock in the WCB basin likely regulates how fast the incision wave is transmitted
649 upstream, while the terrace staircase formation across the basin will mostly respond to
650 the fast-propagating waves that travel through the soft Neogene sediment cover.

651 Regarding the timing of the basin opening, compared to other Cenozoic basins from
652 the Iberian Peninsula, the endo-exhoreic transition of the Duero Basin is likely to have
653 occurred after that of the Ebro Basin (Antón et al., 2019). In the Ebro Basin, the fluvial
654 network attained an advanced phase of adjustment since the opening of the foreland
655 basin towards the Mediterranean Sea (Soria-Jáuregui et al., 2019). Resultant fluvial
656 incision was able to induce as much as 630 m of uplift due to isostatic rebound, which is
657 consistent with an opening age of 12.0–7.5 Ma obtained restoring the flexural isostatic
658 compensation linked to infill erosion (García-Castellanos and Cruz-Larrasoña, 2015).
659 In contrast, the Duero Neogene infill is poorly dissected and it pretty much preserves
660 the pre-opening topography, with an estimated average surface lowering limited to $65 \pm$
661 13 m (Antón et al., 2019). Besides, the Duero river profile remains in disequilibrium
662 illustrating a transient erosive response to the opening (Antón et al., 2014). The
663 comparative analysis of chi-indices and knickpoint distribution for both basins
664 highlights these differences, and the recalculated chi values once the drainage area is
665 removed also supports the hypothesis of a recent endo-exorheic transition of the Duero
666 Basin (Struth et al., 2019). Hence, a basin opening towards the Atlantic Ocean later than
667 ca. 4-5 Ma, derived from our data, agrees with previous interpretations that assume a
668 Plio-Pleistocene age for the basin switching from sedimentation to erosion due to its
669 opening into the Atlantic Ocean (Benito-Calvo and Pérez-González, 2007; Silva et al.,
670 2017; Antón et al., 2019; Cunha et al., 2019).

671 *5.2. Spatial variation of fluvial incision and denudation rates*

672 The CSEB model suggests that the erosive fingerprint of the basin endo-exorheic
673 transition was important at the source area of sediments since at least 2–1 Ma ago,
674 marked by the increase in apparent basin denudation rates and the increased proportion

675 of fresh sediments recorded in the lowest terraces. This interpretation is consistent with
676 Electro Spin Resonance (ESR) chronologies reported for fluvial terraces in the Arlanzón
677 and Arlanza valleys, two tributaries of the Duero river placed more than 130 km
678 upstream from our study area (Table IV and Figure 10). In the Arlanzón River an ESR
679 age of 1.14 ± 0.13 Ma was reported for terrace T3 (+78–70 m), while the inferior levels
680 provided the following results (Moreno et al., 2012): (i) 0.78 ± 0.12 and 0.93 ± 0.10 Ma
681 for terrace T4 (+67–60 m); (ii) 0.70 ± 0.10 Ma for terrace T5 (+54–50 m); (iii) $0.40 \pm$
682 0.09 Ma for terrace T8 (+35–26 m); and (iv) 0.14 ± 0.02 Ma for terrace T11 (+13–12
683 m). Similarly, the ESR chronology of the nearby Arlanza River yielded ages of $0.79 \pm$
684 0.11 Ma for terrace T5 (+79–73 m); 0.70 ± 0.07 Ma for terrace T6 (+67–64 m); $0.35 \pm$
685 0.04 Ma for terrace T10 (+36–33 m); and 0.23 ± 0.03 Ma for terrace T12 (+23–20 m),
686 suggesting similar fluvial evolution in both tributaries (Moreno et al., 2016) (Table IV,
687 Figure 10). In the Esla River, a tributary which converges with the Duero river ~50 km
688 downstream from the study area, thirteen terrace levels were described with the highest
689 terrace located at +160 m (Torrent, 1976). Upper terraces are associated to a Paleo-Esla,
690 which switched its course to the west between ~0.52 Ma and 0.15 Ma (Schaller et al.,
691 2016b). An age of ~1.04 Ma was assigned to the highest level by previous authors,
692 while cosmogenic nuclides analysis in lower fluvial terraces yielded depositional ages
693 of $\sim 0.52 \pm 0.20$ Ma for the youngest Paleo-Esla terrace at +78–76 m and 0.16 to 0.08
694 Ma for the lowest Esla terraces at +64–32 m to +8–7 m (Schaller et al., 2016b) (Table
695 IV and Figure 10). Both datasets support the idea that in the tributary valleys close to
696 the source area of sediments most terraces formed over the last ~1.5–1 Ma, while in our
697 study area the studied terraces were most likely formed since 2.5–1 Ma (depending on
698 the total surface lowering scenario assumed).

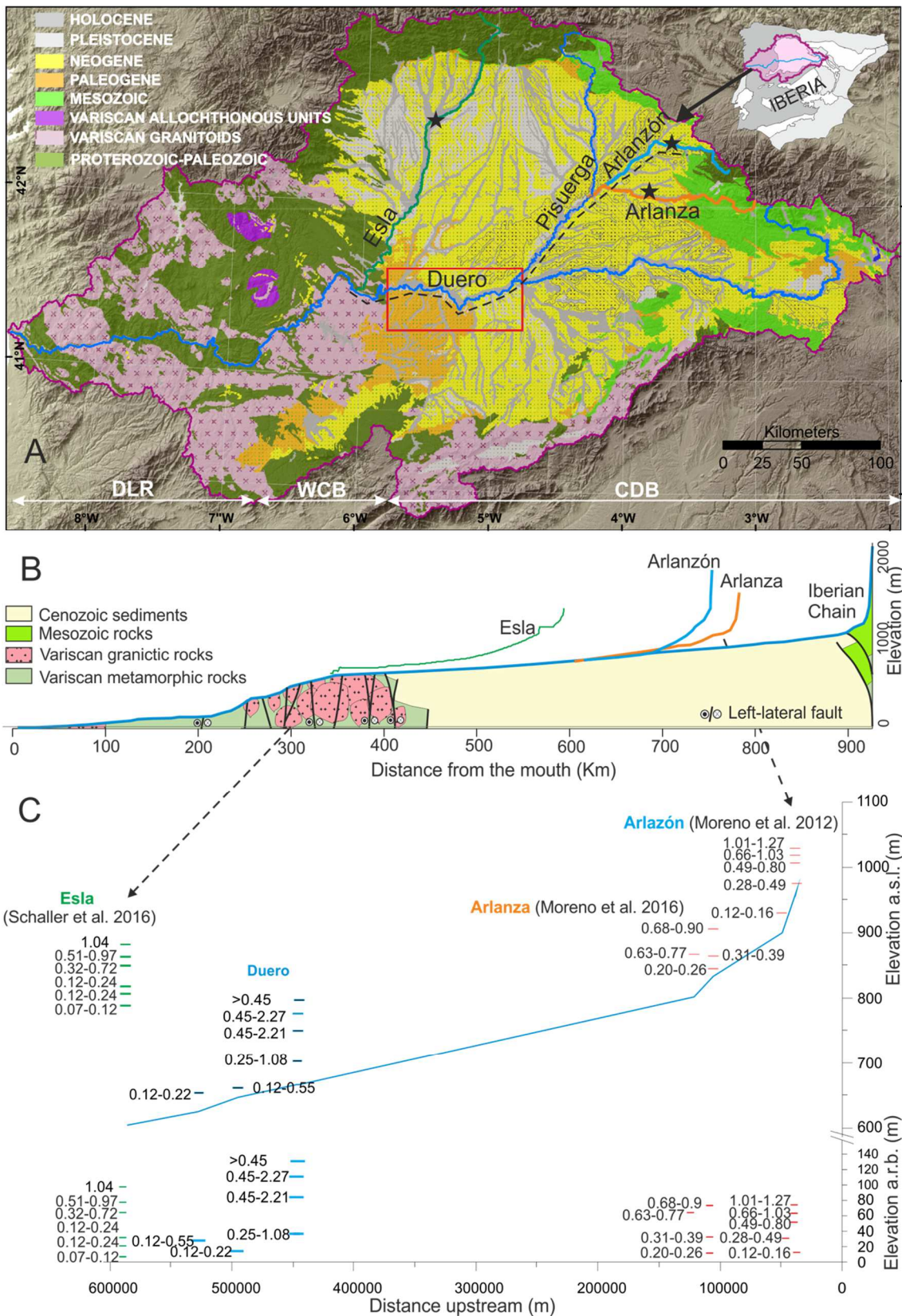
699
700
701
702

Table IV.- Available chronological framework for the Duero fluvial network upstream the Arribes knickzone, including the Arlanzón, Arlanza and Esla tributaries. Incision rate estimations along the main channel for each of these rivers considering available terraces ages and maximum total incision observed for each terrace level at the specific sampling site. Terrace level names according to the references.

| Valley | Terrace level | Terrace height (m) | Age (Ma) | | Incision rate (m/Ma) | | Reference |
|------------|---------------|--------------------|----------|------|----------------------|-----|-------------------------|
| | | | min | max | max | min | |
| Arlanzón | T3 | +78-70 | 1.01 | 1.27 | 77 | 61 | Moreno et al. (2012) |
| | | +67-60 | 0.66 | 0.9 | 102 | 74 | |
| | T5 | +67-60 | 0.83 | 1.03 | 81 | 65 | |
| | | +54-50 | 0.6 | 0.8 | 90 | 68 | |
| | | +54-50 | 0.63 | 0.77 | 86 | 70 | |
| | T8 | +54-50 | 0.49 | 0.67 | 110 | 81 | |
| | | +35-26 | 0.28 | 0.44 | 125 | 80 | |
| | | +35-26 | 0.31 | 0.49 | 113 | 71 | |
| Arlanza | T11 | +13-12 | 0.12 | 0.16 | 108 | 81 | Moreno et al. (2016) |
| | T5 | +79-73 | 0.68 | 0.9 | 116 | 88 | |
| | T6 | +67-64 | 0.63 | 0.77 | 106 | 87 | |
| | T10 | +36-33 | 0.31 | 0.39 | 116 | 92 | |
| | T12 | +23-20 | 0.2 | 0.26 | 115 | 88 | |
| Duero | T3 (3.5 m)* | +112-107 | >0.55 | 2.27 | <202 | 49 | This study |
| | T6 (3 m)* | +85-81 | >0.55 | 2.21 | <153 | 38 | |
| | T10 (3 m)* | +39-34 | 0.55 | 1.08 | 70 | 36 | |
| | T11 (4 m)* | +26-22 | >0.15 | 0.55 | <173 | 47 | |
| | T12 (1.5 m)* | +13-11 | 0.15 | 0.22 | 87 | 60 | |
| | T3 (0.7 m)* | +112-107 | >0.45 | 0.98 | <249 | 115 | |
| | T6 (0.2 m)* | +85-81 | 0.45 | 0.61 | 189 | 139 | |
| | T10 (0.2 m)* | +39-34 | 0.25 | 0.33 | 157 | 120 | |
| | T11 (0.6 m)* | +26-22 | >0.12 | 0.17 | <226 | 152 | |
| | T12 (0.2 m)* | +13-11 | 0.12 | 0.14 | 113 | 92 | |
| Paleo-Esla | G; f | +100-95 | 0.51 | 0.97 | 196 | 103 | Schaller et al. (2016b) |
| | SK; h | +78-76 | 0.32 | 0.72 | 244 | 108 | |
| | | +78-76 | 0.39 | 0.72 | 200 | 108 | |
| Esla | P; j | +32 | 0.12 | 0.24 | 267 | 133 | |
| | T20; l | +22-20 | 0.12 | 0.24 | 183 | 92 | |
| | n | +8-7 | 0.07 | 0.12 | 114 | 67 | |

703

(*) Maximum lowering scenario considered for each terrace surface in the exposure age calculation is provided in brackets.



704

705

706

707

708

709

Figure 10.- Synthesis of available chronological data on fluvial terraces for the Duero river and its tributaries: (A) location of dated terrace sequences in the context of the CDB (the rectangle marks the study area; stars indicate the location of other terrace sequences previously dated along the Esla, Arlanza and Arlanzón streams). (B) Long profile of the Duero river and the tributaries with chronological data on terrace sequences (Esla, Arlanza, Arlanzón). (C) Distribution and age (expressed in Ma) of terraces above

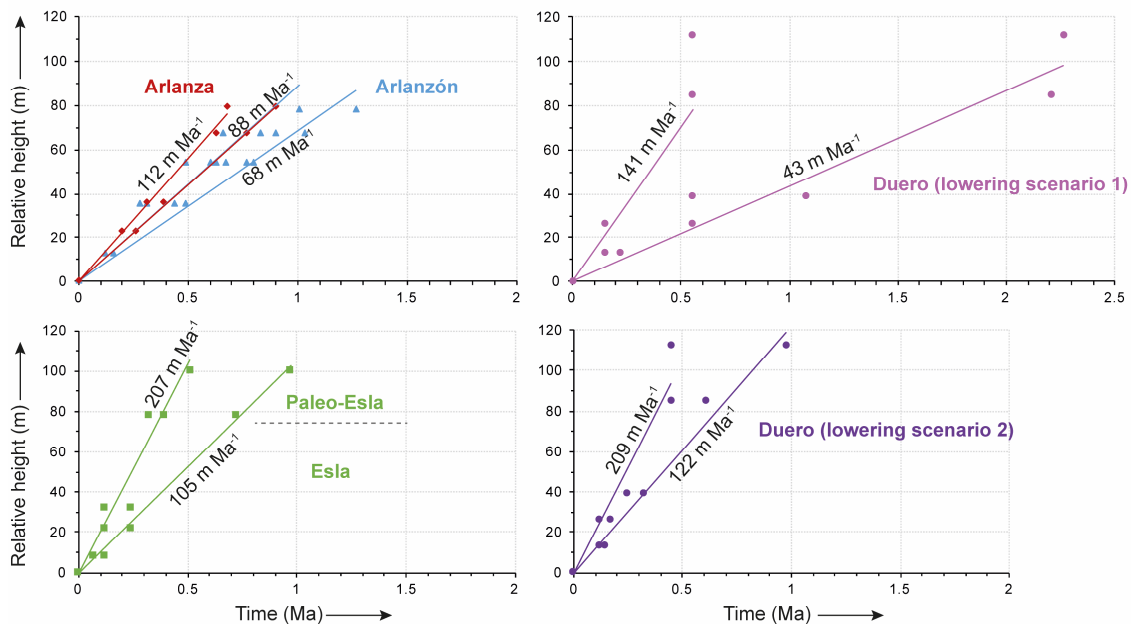
710 the river bed and at their position and elevation over the long profile integrating the Duero and the its
711 tributaries upstream from the WCB up to the Arlanzón. Dashed line in A and arrows in B, show the
712 stretch represented in the integrated long profiles. Chronological data on the Esla river are represented at
713 its confluence's location with the Duero river.

714 River incision rates were estimated in the study area using the maximum relative
715 height of dated terrace levels as a reference for total incision (up to +112 m) and terrace
716 abandonment ages derived from the CSEB dating model (Table IV). Depending on the
717 lowering scenario considered (Figure 11), time-averaged incision rates deduced from
718 linear adjustment of dated terrace values would range between ca. 43–141 m·Ma⁻¹ since
719 2.3 Ma (lowering scenario #1), or 122–209 m·Ma⁻¹ since 1 Ma (lowering scenario #2).
720 These time-averaged incision values obtained close to the basin opening/overspill point
721 seem in turn in agreement with the values obtained upstream. Close to the source area in
722 the Iberian Chain, total incision along the Arlanzón and Arlanza tributaries attained up
723 to 79–78 m over the last 1Ma, involving time-averaged incision rates in the order of 68–
724 88 m·Ma⁻¹ and 88–112 m·Ma⁻¹, respectively (Figure 11). In contrast, the Esla River
725 attained a total incision up to 100 m for the same period of time as reported by Schaller
726 et al. (2016a), involving time averaged incision rates in the range 105–207 m·Ma⁻¹ over
727 the last 1 Ma, which are comparable or slightly lower than those obtained in our study
728 area using the soil-based lowering scenario. These results support the diachronous
729 character of terraces formed through knickpoint propagation as demonstrated in other
730 studies (e.g. Stokes et al., 2002; Rixhon et al., 2011; Baynes et al., 2015; Finnegan,
731 2013). However, the chronological data on time transgressive formation of terraces and
732 basin denudation in the Duero catchment allow further interpretations to understand
733 general-patterns and rates of landscape adjustment associated to basin scale endo-
734 exorheic transitions.

735
736
737

Table V. - Summary of denudation rates and time-averaged incision rates in the Duero, Esla, Arlanza and Arlanzón sites (compiled in Table IV) considering different time periods. Lowering scenarios in the Duero River are based on terrace surface topography (1) and soils (2).

| Time | Duero (scenario 1) | Duero (scenario 2) | Esla | Arlanza | Arlanzón |
|------------------|---|--|---|---|---|
| >3.5 Ma | Basin denudation rates <6 m/Ma (based on inherited ^{10}Be and ^{26}Al from terraces T2, T3 and T6) | | Possibly low basin average denudation rates (based on high ^{10}Be inheritances between 0.14 and 0.3 M atoms/g from terraces in Schaller et al., 2016a) | Possibly slow basin denudation rates, as Arlanza and Arlanzón are inside the catchment of T2, T3, T6, T10, T11 and T12. | |
| Since 2-1Ma | Basin denudation rates rose between 8 and 13 m/Ma (based on inherited ^{10}Be and ^{26}Al from terraces T10, T11 and T12) | Incision rates between 36-49 to <202 m/Ma (based on maximum ^{10}Be and ^{26}Al deposition ages of T3, T6 and T10) | | | |
| Since 1-0.6Ma | Incision rates of 36-70 m/Ma (based on ^{10}Be and ^{26}Al deposition ages of T10) | Incision rates of 115- <249 m/Ma (based on ^{10}Be and ^{26}Al deposition ages of T3) | Incision rates of 103-196 m/Ma based on terrace ^{10}Be deposition ages of paleo-Esla terraces (Schaller et al., 2016b). | Incision rates c. 87-116 m/Ma based on ESR age of terraces T5 and T6 (Moreno et al., 2016) | Incision rates c. 61-102 m/Ma based on ESR ages of terraces T3, T4 and T5 (Moreno et al., 2012) |
| Since 0.6-0.2 Ma | Incision rates of <173 m/Ma (based on ^{10}Be and ^{26}Al deposition ages of T11) | Incision rates of 120-189 m/Ma (based on ^{10}Be and ^{26}Al deposition ages of T6 and T10) | Incision rates c.108-200 m/Ma (based on terrace ^{10}Be deposition ages in Schaller et al., 2016b). Basin denudation of 60-56 m/Ma (Schaller et al., 2016b) | Incision rates of 88-116 m/Ma based on ESR age of +64m terraces (Moreno et al., 2016) | Incision rates up to 125 m/Ma based on ESR ages of terraces T5, and T8 (Moreno et al., 2012) |
| Since <0.2 Ma | Incision rates of 60-87 m/Ma (based on ^{10}Be and ^{26}Al minimum deposition age of T12) | Incision rates of ca. 92 to <226 m/Ma (based on ^{10}Be and ^{26}Al minimum deposition age of T11 and T12) | Incision rates between 67 and 114 m/Ma based on ^{10}Be deposition age of terrace 12ESL007 (Schaller et al., 2016b). Basin denudation rates of 33-56 m/Ma (Schaller et al., 2016a) | — | Incision rate of 81-108 m/Ma based on ESR age of terrace T11 (Moreno et al., 2012) |



738
739
740

Figure 11.- Comparison between terrace sequences preserved at specific sampling sites along the Arlanzón, Arlanza and Esla tributaries with that recorded along the main Duero river in our study area,

741 based on datasets compiled in Table V. For the Duero river, the two different lowering scenarios
742 discussed in the main text are provided, which are based on terrace surface topography (1) and soil
743 characteristics (2). Each pair of regression lines represent average incision rates at each site in the basin
744 using the full dataset locally available.

745 Cyclic fluvial aggradation and entrenchment episodes are frequently interpreted as
746 the response to sustained base-level lowering driven by a combination of tectonic and/or
747 climatic fluctuations (e.g. Bridgland and Westaway, 2008; Cunha et al. 2008). The
748 Duero Basin occupies a relatively stable tectonic setting where evidence of significant
749 tectonic uplift since the late Miocene is absent (De Vicente and Vegas, 2009; Antón et
750 al., 2010). Chronological data on fluvial terraces do not favor a straightforward
751 interplay between climate and terrace formation. Nevertheless, the base level lowering
752 associated at the basin opening seems the main mechanism linked to basin infill
753 dissection and terrace staircase development. In a similar context, Bartz (2019) rule out
754 climate as the main driver mechanism for fluvial aggradation in the Triffa basin (NE
755 Morocco), suggesting that basin scale capture events might dominate a fluvial transient
756 response. Previous works (e.g. Paola et al., 1992; Beaumont et al., 2000), indicate that
757 each system has an intrinsic time response to recover the equilibrium after a climatic
758 perturbation or a change in drainage connectivity. This time is scale-dependent but falls
759 often in the order of millions of years (Whipple and Tucker, 1999; Pazzaglia, 2003,
760 Whipple, 2001; García-Castellanos and Larrasoaña, 2015). Even for much smaller
761 basins of 10 and 70 km² in Hatay Graben (Turkey) and the Apennines, Whittaker and
762 Boulton (2012) estimate a fluvial response time in the order of 3–1 Ma. In the Duero
763 river case, the configuration of the crystalline hard bedrock at the WCB might have
764 contributed in delaying the time needed to recover a steady-state profile.

765 The recorded eastward progression of the incision wave generated in the opening
766 area (Table VI), illustrates the erosional pattern expected in continental basins that
767 underwent an endorheic to exorheic transition, (e.g. Antón et al., 2019; Bartz, 2019;
768 Mather, 2000; Stokes et al., 2002, 2018; Soria-Jáuregui et al., 2019). A strong coupling
769 between the rate of fluvial downcutting and orbital-forcing has been suggested for the
770 Tagus and the Duero rivers, particularly since the establishment of the 100 ka
771 eccentricity cycles (Silva et al., 2017). Our chronological results favor an increase of
772 apparent basin denudation since ~2 Ma, but do not allow an accurate interpretation of
773 the interplays between climate and terrace formation. We assume that changes in
774 sediment supply related to climate cyclicity are superimposed onto the long-term base
775 level lowering, which dominates the fluvial entrenchment in the area. The base level

776 drop resulting from the onset of exorheism generates knickpoint wave trains
777 propagating upstream along the drainage system (Struth et al., 2019). In the Duero,
778 immediately downstream of the study area, the incision is limited by the resistant
779 lithology at the Arribes gorge (WCB, Figure 10), which regulates the transmission of
780 successive knickpoint waves upstream. As the Duero attains incision at the basin outlet
781 (WCB), the erosive wave propagates towards the basin center increasing the profile
782 gradient. While the knickpoint progresses upstream, the fluvial system aggrades
783 downstream to progressively balance the channel gradient. Successive incision waves,
784 due to progressive incision at the basin outlet, will result in fluvial downcutting with the
785 development of the inset Pleistocene river terrace sequence at the basin center and the
786 propagation of the erosional signal along the tributary network to the catchment divide.
787 This model is consistent with an enhanced erosion in the Esla catchment allowing
788 higher incision rates and total incision (highest terrace at +100 m) than in the Arlanza-
789 Arlanzón system placed further upstream (highest terrace ~80 m; Figures 10 and 11).
790 Also, significant differences in terrace patterns and landscape dissection are observed in
791 the main trunk (Rodríguez-Rodríguez et al., 2020), with the highest terraces only
792 preserved upstream at the basin center (Figure 2). At a basin scale, the relatively low
793 average denudation rates derived from the upper terraces are consistent with a null or
794 scarce transmission of the erosive wave nucleated at the opening site along the
795 catchment at that stage. In contrast, by the time of the lowest terraces formation (T10,
796 T11 and T12) denudation rates doubled, suggesting the establishment of much more
797 erosive conditions at basin scale and the arrival of the enhanced erosional signal to the
798 basin source.

799 The Cenozoic Duero basin is an exceptional example to understand the evolution of
800 sedimentary basins and longer-term landscape response associated to a continental scale
801 drainage reorganization. Results provide a chronological framework for the terrace
802 sequence and illustrate the main role of autogenic mechanisms in landscape dissection
803 and terrace staircase formation in response to basin-scale endorheic to exorheic drainage
804 transition.

805 **6. Conclusions**

806 Paired ^{10}Be - ^{26}Al concentrations measured in six terrace depth profiles of the Duero
807 fluvial terrace staircase upstream from the western margin of the Cenozoic basin

808 provide important insights about the timing of the endo-exorheic transition and
809 subsequent basin evolution:

- 810 1) Inherited ^{10}Be - ^{26}Al concentrations suggest an increase in basin denudation rates
811 after the basin opening to the Atlantic Ocean. Basin average denudation rates
812 remained relatively low ($<3\text{--}6\text{ m}\cdot\text{Ma}^{-1}$) until at least 3.5 Ma, showing higher
813 proportions of recycled sediments, and then experienced an acceleration at ca.
814 2–1 Ma ($8\text{--}13\text{ m}\cdot\text{Ma}^{-1}$).
- 815 2) Terrace surface exposure ages obtained with the CSEB model can be
816 constrained by limiting the total amount of surface lowering based on
817 geomorphic and soil indicators. Future studies based on alternative dating
818 methods might help to better constrain the most probable post-depositional
819 lowering scenario for the studied terraces. In any case, the CSEB model favors
820 Pleistocene ages ($<2.5\text{ Ma}$) for the terraces belonging to the Duero staircase.
- 821 3) The apparent change in basin-scale denudation rates is in agreement with the
822 propagation of an eastward erosive wave through the study area as proposed by
823 Struth et al. (2019), nucleated at the western fringe of the basin during the endo-
824 exorheic transition. This wave might have arrived at the basin source between
825 ~ 1 to 2 Ma ago, being T10 the oldest terrace clearly containing sediments that
826 record the starting of the upper Duero incision in bedrock. This is consistent
827 with previous chronologies reported for some of the oldest terraces preserved in
828 tributary rivers like the Arlanzón, Arlanza and Esla, where the oldest terrace
829 ages are around 1 Ma.
- 830 4) Time-averaged incision rates over the last million years display the highest
831 values close to the opening site of the CDB (122 to $<250\text{ m}\cdot\text{Ma}^{-1}$ in the Duero
832 River; $105\text{--}207\text{ m}\cdot\text{Ma}^{-1}$ in the Esla River), and the lowest values close to the
833 eastern boundary of the catchment ($68\text{--}88\text{ m}\cdot\text{Ma}^{-1}$ in the Arlanzón River).

834 Altogether, these findings support the diachronous character of landscape
835 dissection through knickpoint propagation from the opening zone and illustrate the time
836 transgressive formation of terraces along the Duero catchment.

837 **Acknowledgements**

838 This is a MITE contribution (Spanish Government *Plan Estatal de Investigación*
839 *Científica y Técnica y de Innovación*, CGL2014-59516 & PR2011-0044). At the time of
840 paper writing, L. Rodríguez-Rodríguez was recipient of an outgoing post-doctoral grant

841 of the Clarín-Cofund program (Ref. ACA-17-19), financed jointly by the regional
842 government of Principality of Asturias and the 7th WP of the European Union–Marie
843 Curie Actions. The ASTER AMS national facility (CEREGE, Aix en Provence) is
844 supported by the INSU/CNRS, the ANR through the "Projets thématiques d'excellence"
845 program for the "Equipements d'excellence" ASTER-CEREGE action and IRD.
846 Candela Pastor-Martín is thanked for the GIS technical support (funded under grant
847 PEJ-2014-A-93258). We thank Martin Stokes and Zsófia Ruzsiczay-Rüdiger for their
848 constructive reviews on the manuscript, which helped us to improve the initial version.
849 We are also thankful to the enterprises Arentis Aridos S.L., Barbado Martín S.L.,
850 Aridos Sola e Hijos S.L., and Jose Isidro Torres S.L. for allowing us to sample fluvial
851 sediments in exposed terrace sections at their exploitation quarries.

852 **References**

- 853 Alonso, J.L., Pulgar, J.A., García-Ramos, J.C., Barba, P., 1996. Tertiary basins and
854 Alpine tectonics in the Cantabrian Mountains (NW Spain). In: Friend, P.F., Dabrio,
855 C.J. (Eds.), Tertiary Basins of Spain: the stratigraphic record of crustal kinematics.
856 Cambridge University Press, Cambridge, pp. 214–227.
- 857 Alonso-Gavilán, G., Armenteros, I., Carballeira, J., Corrochano, A., Huerta, P.,
858 Rodríguez, J., 2004. Cuenca del Duero. In: Vera, J.A. (Ed.), Geología de España.
859 IGME, Madrid, pp- 550-556.
- 860 Alonso Gavilan, G., Dabrio, C.J., Mediavilla, R.M., Armenteros, I., 1989. Procesos
861 sedimentarios y desarrollo de Sand Flats en ríos arenosos del Eoceno del suroeste de
862 la depresion del Duero. *Studia Geologica Salmanticensia*, Extraordinario No. 5, 159-
863 176.
- 864 Alonso-Zarza, A.M., 2003. Palaeoenvironmental significance of palustrine carbonates
865 and calcretes in the geological record. *Earth-Science Reviews* 60, 261-298.
- 866 Alonso-Zarza, A.M., Armenteros, I., Braga, J.C., Munoz, A., Pujalte, V., Ramos, E.,
867 Aguirre, J., Alonso Gavilan, G., Arenas, C., Baceta, J.I., Carballeira, J., Calvo, J.P.,
868 Corrochano, A., Fornos, J.J., Gonzalez, A., Luzon, A., Martin, J.M., Pardo, G.,
869 Payros, A., Perez, A., Pomar, L., Rodriguez, J.M., Villena, J., 2002. Tertiary. In: W.
870 Gibbons, T. Moreno (Eds.), *The geology of Spain*. Geological Society, Bath, United
871 Kingdom, pp. 293-334.
- 872 Antón, L., Muñoz-Martín, A., De Vicente, G., 2010. Alpine paleostress reconstructions
873 and active faulting in Western Iberia. *Central European Journal of Geosciences* 2,
874 152-164.

875 Antón, L., De Vicente, G., Muñoz-Martín, A., Stokes, M., 2014. Using river long
876 profiles and geomorphic indices to evaluate the geomorphological signature of
877 continental scale drainage capture, Duero basin (NW Iberia). *Geomorphology* 206,
878 250-261.

879 Antón, L., Muñoz-Martín, A., De Vicente, G., 2019. Quantifying the erosional impact
880 of a continental scale drainage capture in the Duero Basin (NW Iberia). *Quaternary*
881 *Research*, 91(2), 457-471.

882 Antón, L., Rodés, A., De Vicente, G., Pallàs, R., Garcia-Castellanos, D., Stuart, F.M.,
883 Braucher, R., Bourlès, D., 2012. Quantification of fluvial incision in the Duero Basin
884 (NW Iberia) from longitudinal profile analysis and terrestrial cosmogenic nuclide
885 concentrations. *Geomorphology*, 165–166, 50-61.

886 Arnold, M., Merchel, S., Bourlès, D., Braucher, R., Benedetti, L., Finkel, R.C.,
887 Aumaître, G., Gott dang, A., Klein, M., 2010. The French accelerator mass
888 spectrometry facility ASTER: Improved performance and developments. *Nuclear*
889 *Instruments and Methods in Physics Research B*, 268, 1954-1959.

890 Balco, G., 2017. Production rate calculations for cosmic-ray-muon-produced ^{10}Be and
891 ^{26}Al benchmarked against geological calibration data. *Quaternary Geochronology* 39,
892 150-173.

893 Balco, G., Stone, J.O., Lifton, N.A., Dunai, T.J., 2008. A complete and easily accessible
894 means of calculating surface exposure ages or erosion rates from ^{10}Be and ^{26}Al
895 measurements. *Quaternary Geochronology*, 3 (3), 174-195.

896 Bartz, M., 2019. Quaternary fluvial environments in NE Morocco inferred from
897 geochronological and sedimentological investigations. *E&G Quaternary Science*
898 *Journal* 68, 1-4.

899 Baynes, E.R.C., Attal, M., Niedermann, S., Kirstein, L.A., Dugmore, A.J., Naylor, M.,
900 2015. Erosion during extreme flood events dominates Holocene canyon evolution in
901 northeast Iceland. *Proceedings of the National Academy of Sciences*, 112 (8), 2355-
902 2360.

903 Beamoud, E., Garcés, M., Montes, M., Nozal, F., Calvo, J. P., López-Olmedo, F.,
904 Luengo, J., 2006. Magnetoestratigrafía del Mioceno de las cuencas del Tajo y del
905 Duero. *Proceedings of the IV Simposio de Paleomagnetismo Ibérico*
906 (MAGIBER), vol. 4, pp. 9-12.

907 Beaumont, C., Kooi, H., Willett, S., 2000. Coupled tectonic-surface process models
908 with applications to rifted margins and collisional orogens. In: Summerfield, M.A.

909 (Ed.), *Geomorphology and Global Tectonics*. Chirchester, John Wiley and Sons, pp.
910 28–55.

911 Benito-Calvo, A., Pérez-González, A., 2007. Erosion surfaces and Neogene landscape
912 evolution in the NE Duero Basin (north-central Spain). *Geomorphology* 88, 226-241.

913 Benito-Calvo, A., Pérez-González, A. y Pares, J.M., 2008. Quantitative Reconstruction
914 of Late Cenozoic Landscapes: A Case Study in the Sierra de Atapuerca (Burgos,
915 Spain). *Earth Surface Processes and Landforms* 33 (2), 196-208.

916 Braucher, R., Merchel, S., Borgomano, J., Bourlès, D., 2011. Production of cosmogenic
917 radionuclides at great depth: A multi element approach. *Earth and Planetary Science*
918 *Letters* 309 (1-2), 1-9.

919 Bridgland, D.R., Westaway, R., 2008. Preservation patterns of Late Cenozoic fluvial
920 deposits and their implications: Results from IGCP 449. *Quaternary International*
921 189, 5-38.

922 Capote, R., Insua Arévalo, J.M., Martínez-Díaz, J.J., Martín-González, F., Tsige, M.,
923 2002. La Sierra de Cártama: Pliegue con actividad reciente en las Béticas
924 Occidentales (Hoya de Málaga). *Geogaceta* 31, 135–138.

925 Cunha, P., Martins, A.A., Huot, S., Murray, A., Raposo, L., 2008. Dating the Tejo river
926 lower terraces in the Rodao area (Portugal) to assess the role of tectonics and uplift.
927 *Geomorphology* 64, 271-298.

928 Cunha, P., Martins, A.A., Gomes, A., Stokes, M., Cabral, J., Lopes, F.C., Pereira, D., de
929 Vicente, G., Builaert, J.P., Murray, A.S., Antón, L., 2019. Mechanism and age
930 estimates of continental-scale endorheic to exorheic drainage transition: Douro
931 River, Western Iberia. *Global and Planetary Change* 181,
932 <https://doi.org/10.1016/j.gloplacha.2019.102985>

933 Chmeleff, J., von Blanckenburg, F., Kossert, K., Jakob, D., 2010. Determination of the
934 ¹⁰Be half-life by multicollector ICP-MS and liquid scintillation counting. *Nuclear*
935 *Instruments and Methods in Physics Research Section B: Beam Interactions with*
936 *Materials and Atoms*, 268 (2), 192-199.

937 Demoulin, A., Mather, A., Whittaker, A., 2017. Fluvial archives, a valuable record of
938 vertical crustal deformation. *Quaternary Science Reviews* 166, 10-37.

939 De Vicente, G., Vegas, R., 2009. Large-scale distributed deformation controlled
940 topography along the western Africa-Eurasia limit: Tectonic constraints.
941 *Tectonophysics* 474 (1-2), 124-143.

942 Dunai, T.J., 2010. *Cosmogenic Nuclides: Principles, concepts and applications in the*
943 *Earth Surface Sciences*. Cambridge University Press, 187 pp.

944 Finnegan, N.J., 2013. Interpretation and downstream correlation of bedrock river terrace
945 treads created from propagating knickpoints. *Journal of Geophysical Research: Earth*
946 *Surface*, 118 (1), 54-64.

947 Friend, P.F., Dabrio, C.J., 1996. *Tertiary basins of Spain: the stratigraphic record of*
948 *crustal kinematics*. Cambridge University Press, Cambridge.

949 García-Castellanos, D., Larrasoaña, J.C., 2015. Quantifying the post-tectonic
950 topographic evolution of closed basins: The Ebro basin (northeast Iberia). *Geology*
951 43, 663-666.

952 García-Castellanos, D., Vergés, J., Gaspar-Escribano, J., Cloetingh, S., 2003. Interplay
953 between tectonics, climate, and fluvial transport during the Cenozoic evolution of the
954 Ebro Basin (NE Iberia). *Journal of Geophysical Research: Solid Earth* 108, 2347.

955 Gómez-Ortiz, D., Tejero-Lopez, R., Babín-Vich, R., Rivas-Poncé, A., 2005. Crustal
956 density structure in the Spanish Central System derived from gravity data analysis
957 (central Spain). *Tectonophysics* 403, 131–149.

958 González de Vallejo, L.I., 2002. *Ingeniería geológica*. Pearson Prentice Hall, 744 pp.

959 Gosse, J.C., Phillips, F., 2001. Terrestrial in situ cosmogenic nuclides: theory and
960 application. *Quaternary Science Reviews*, 20, 1475-1560.

961 Granger, D.E., Muzikar, P.F., 2001. Dating sediment burial with in situ-produced
962 cosmogenic nuclides: theory, techniques, and limitations. *Earth and Planetary*
963 *Science Letters* 188, 269-281.

964 He, P., Wang, X., Song, C., Wang, Q., Deng, L., Zhong, S., 2017. Cenozoic evolution
965 of the Western Qinling Mt. Range based on thermochronologic and sedimentary
966 records from the Wudu Basin, NE Tibetan Plateau. *Journal of Asian Earth Sciences*
967 138, 484-494.

968 Heidarzadeh, G., Ballato, P., Hassanzadeh, J., Ghassemi, M.R., Strecker, M.R., 2017.
969 Lake overflow and onset of fluvial incision in the Iranian Plateau: Insights from the
970 Mianeh Basin. *Earth and Planetary Science Letters* 469, 135-147.

971 Heisinger, B., Lal, D., Jull, A. J. T., Kubik, P., Ivy-Ochs, S., Knie, K. and Nolte, E.,
972 2002a. Production of selected cosmogenic radionuclides by muons: 2. Capture of
973 negative muons, *Earth and Planetary Science Letters* 200, 357–369.

974 Heisinger, B., Lal, D., Jull, A. J. T., Kubik, P., Ivy-Ochs, S., Neumaier, S., Knie, K.,
 975 Lazarev, V. and Nolte, E., 2002b. Production of selected cosmogenic radionuclides
 976 by muons 1. Fast muons, *Earth and Planetary Science Letters* 200, 345-355.

977 Krijgsman, W., Garcés, M., Langereis, C.G., Daams, R., van Dam, J., van der Meulen,
 978 A.J., Agustí, J., Cabrera, L., 1996. A new chronology for the middle to late Miocene
 979 continental record in Spain. *Earth and Planetary Science Letters* 142, 367-380.

980 Lal, D., 1991. Cosmic ray labeling of erosion surfaces: in situ nuclide production rates
 981 and erosion models. *Earth and Planetary Science Letters*, 104, 424-439.

982 Lal, D., Arnold, J.R., 1985. Tracing quartz through the environment. *Proceedings of the*
 983 *Indian Academy of Sciences-Earth and Planetary Sciences*, 94, Issue 1, pp. 1-5.

984 Mather, A.E., 2000. Adjustment of a drainage network to capture induced base-level
 985 change: an example from the Sorbas Basin, SE Spain. *Geomorphology* 34, 271-289.

986 Mather, A.E., Stokes, M., Whitfield, E., 2017. River terraces and alluvial fans: The case
 987 for an integrated Quaternary fluvial archive. *Quaternary Science Reviews* 166, 74-
 988 90.

989 Mediavilla, R.U., Dabrio, C.J., 1989. Análisis sedimentológico de los conglomerados de
 990 Tariago (Unidad 4, Neógeno de la depresión del Duero). *Studia Geologica*
 991 *Salmanticensia*, Extraordinario No. 5, 293-310.

992 Mediavilla, R., Dabrio, C.J., Martín-Serrano, A., Santisteban, J.J., 1996. Lacustrine
 993 Neogene systems of the Duero Basin: evolution and controls. In: Friend, P.F.,
 994 Dabrio, C.J. (Eds.), *Tertiary Basins of Spain: the stratigraphic record of crustal*
 995 *kinematics*. Cambridge University Press, Cambridge, pp. 228-236.

996 Moreno, D., Falguères, C., Pérez-González, A., Duval, M., Voinchet, P., Benito-Calvo,
 997 A., Ortega, A.I., Bahain, J.J., Sala, R., Carbonell, E., Bermúdez de Castro, J.M.,
 998 Arsuaga, J.L., 2012. ESR chronology of alluvial deposits in the Arlanzón valley
 999 (Atapuerca, Spain): Contemporaneity with Atapuerca Gran Dolina site. *Quaternary*
 1000 *Geochronology* 10, 418-423.

1001 Moreno, D., Benito-Calvo, A., Falguères, C., Voinchet, P., Pérez-González, A., 2016.
 1002 Preliminary Electron Spin Resonance (ESR) dating of Arlanza valley (NE Duero
 1003 Basin, Burgos, Spain). XIV Reunión Nacional de Geomorfología, abstracts volume,
 1004 Málaga, 391-398.

1005 Nishiizumi, K., 2004. Preparation of ²⁶Al AMS standards. *Nuclear Instruments and*
 1006 *Methods in Physics Research Section B* 223, 388-392.

- 1007 Paola, C., Heller, P.L., Angevine, C.L. 1992. The large-scale dynamics of grain size
1008 variation in alluvial basins, 1: Theory. *Basin Research* 4, 73–90.
- 1009 Pazzaglia, F.K. 2003. Landscape evolution models. *Developments in Quaternary*
1010 *science* 1, 247-274.
- 1011 Pérez-González, A., 1982. El Cuaternario de la región central de la Cuenca del Duero y
1012 sus principales rasgos geomorfológicos, I Reunión sobre la Geología de la Cuenca
1013 del Duero. IGME, Salamanca, pp. 641-659.
- 1014 Richardson, N.J., Densmore, A.L., Seward, D., Fowler, A., Wipf, M., Ellis, M.A.,
1015 Yong, L., Zhang, Y., 2008. Extraordinary denudation in the Sichuan Basin: Insights
1016 from low-temperature thermochronology adjacent to the eastern margin of the
1017 Tibetan Plateau. *Journal of Geophysical Research: Solid Earth*, 113, B04409.
- 1018 Rixhon, G., Braucher, R., Bourlès, D., Siame, L., Bovy, B., Demoulin, A., 2011.
1019 Quaternary river incision in NE Ardennes (Belgium)–Insights from $^{10}\text{Be}/^{26}\text{Al}$
1020 dating of river terraces. *Quaternary Geochronology*, 6 (2), 273-284.
- 1021 Rodés, Á., Pallàs, R., Ortuño, M., García-Melendez, E., Masana, E., 2014. Combining
1022 surface exposure dating and burial dating from paired cosmogenic depth profiles.
1023 Example of El Límite alluvial fan in Huércal-Overa basin (SE Iberia). *Quaternary*
1024 *Geochronology*, 19, 127-134.
- 1025 Rodés, A., Pallàs, R., Braucher, R., Moreno, X., Masana, E., Bourlés, D.L., 2011. Effect
1026 of density uncertainties in cosmogenic ^{10}Be depth-profiles: Dating a cemented
1027 Pleistocene alluvial fan (Carboneras Fault, SE Iberia). *Quaternary Geochronology* 6,
1028 186-194.
- 1029 Rodríguez-Rodríguez, L., Antón, L., Pallàs, R., García-Castellanos, D., Jiménez-Munt,
1030 I., Pastor-Martín, C., 2020. A GIS method to identify flat surfaces and restore relict
1031 fluvial long-profiles from terrace remnants gives new clues on how large basins
1032 respond to endo-exorheic transitions (Duero Basin, Iberian Peninsula). *Earth Surface*
1033 *Processes and Landforms* 45 (4), 1013-1027.
- 1034 Santisteban, J.I., Schulte, L., 2007. Fluvial networks of the Iberian Peninsula: a
1035 chronological framework. *Quaternary Science Reviews* 26, 2738-2757.
- 1036 Santisteban, J.I., Alcalá, L., Mediavilla, R.M., Alberdi, M.T., Luque, L., Mazo, A.,
1037 Miguel, I., Morales, J., Pérez, B., 1997. El Yacimiento de Tariego de Cerrato: El
1038 inicio de la red de drenaje actual en el sector central de la Cuenca del Duero.
1039 *Cuadernos de Geología Ibérica* 22, 431-446.

1040 Schaller, M., Ehlers, T.A., Stor, T., Torrent, J., Lobato, L., Christl, M., Vockenhuber,
1041 C., 2016a. Spatial and temporal variations in denudation rates derived from
1042 cosmogenic nuclides in four European fluvial terrace sequences. *Geomorphology*
1043 274, 180-192.

1044 Schaller, M., Ehlers, T.A., Stor, T., Torrent, J., Lobato, L., Christl, M., Vockenhuber,
1045 C., 2016b. Timing of European fluvial terrace formation and incision rates
1046 constrained by cosmogenic nuclide dating. *Earth and Planetary Science Letters* 451,
1047 221-231.

1048 Silva, P.G., Roquero, E., López-Recio, M., Huerta, P., Martínez-Graña, A.M., 2017.
1049 Chronology of fluvial terrace sequences for large Atlantic rivers in the Iberian
1050 Peninsula (Upper Tagus and Duero drainage basins, Central Spain). *Quaternary*
1051 *Science Reviews*, 166, 188-203.

1052 Soil Survey Staff, 2015. Illustrated guide to soil taxonomy, version 2. U.S. Department
1053 of Agriculture, Natural Resources Conservation Service, National Soil Survey
1054 Center, Lincoln, Nebraska. USDA, 2015. Illustrated guide to soil taxonomy

1055 Spencer, J.E., Pearthree, P.A., 2001. Headward erosion versus closed-basin spillover as
1056 alternative causes of Neogene capture of the ancestral Colorado River by the Gulf of
1057 California. In Young, R.A., Spamer, E.E., (Eds.), *The Colorado River: Origin and*
1058 *Evolution: Grand Canyon, Arizona*, Grand Canyon Association Monograph 12, p.
1059 215–222.

1060 Soria-Jáuregui, Á, Jiménez-Cantizano, F., & Antón, L. (2019). Geomorphic and
1061 tectonic implications of the endorheic to exorheic transition of the Ebro River system
1062 in northeast Iberia. *Quaternary Research*, 91 (2), 472-492.

1063 Stokes, M., Mather, A.E., Harvey, A.M., 2002. Quantification of river-capture-induced
1064 base-level changes and landscape development, Sorbas Basin, SE Spain. *Geological*
1065 *Society, London, Special Publications* 191, 23-35.

1066 Stokes, M., Mather, A.E., Rodés, A., Kearsley, S., Lewin, S., 2018. Anatomy, age and
1067 origin of an intramontane top basin surface (Sorbas Basin, Betic Cordillera, SE
1068 Spain). *Quaternary*1 (2), 15.

1069 Stone, J., 2000. Air pressure and cosmogenic isotope production. *Journal of*
1070 *Geophysical Research*, 105, 23753-23759.

1071 Struth, L., Garcia-Castellanos, D., Viaplana-Muzas, M., Vergés, J., 2019. Drainage
1072 network dynamics and knickpoint evolution in the Ebro and Duero basins: From
1073 endorheism to exorheism. *Geomorphology* 327, 554-571.

- 1074 Torrent, J., 1976. Soil development in a sequence of river terraces in northern Spain.
1075 CATENA, 3 (1), 137-151.
- 1076 Whipple, K.X., 2001. Fluvial landscape response time: how plausible is steady-state
1077 denudation? American Journal of Science 301 (4–5), 313–325.
- 1078 Whipple, K.X., Tucker, G.E., 1999. Dynamics of the stream power river incision model:
1079 implications for height limits of mountain ranges, landscape response time scales and
1080 research needs. Journal of Geophysical Research 104, 17661–17674.
- 1081 Whittaker, A.C., Boulton, S.J. 2012. Tectonic and climatic controls on knickpoint
1082 retreat rates and landscape response times. Journal of Geophysical research 117,
1083 F02024.
- 1084 Yu, X., Guo, Z., Fu, S., 2015. Endorheic or exorheic: differential isostatic effects of
1085 Cenozoic sediments on the elevations of the cratonic basins around the Tibetan
1086 Plateau. Terra Nova 27, 21-27.